Lead-Free MDABCO-NH_4I_3 Perovskite Crystals Embedded in Electrospun Nanofibers

Rosa M. F. Baptista [1], Gonçalo Moreira [1], Bruna Silva [1], João Oliveira [1], Bernardo Almeida [1], Cidália Castro [2], Pedro V. Rodrigues [2], Ana Machado [2], Michael Belsley [1,*] andEtelvina de Matos Gomes [1]

[1]Centre of Physics of Minho and Porto Universities (CF-UM-UP), Campus de Gualtar, University of Minho, 4710-057 Braga, Portugal

[2]Institute for Polymers and Composites, Campus de Azurém, University of Minho, 4800-058 Guimarães, Portugal

Abstract

In this work, we introduce lead-free organic ferroelectric perovskite N-methyl-N'-diazabicyclo[2.2.2]octonium)–ammonium triiodide (MDABCO-NH_4I_3) nanocrystals embedded in three different polymer fibers fabricated by the electrospinning technique, as mechanical energy harvesters. Molecular ferroelectrics offer the advantage of structural diversity and tunability, easy fabrication, and mechanical flexibility. Organic–inorganic hybrid materials are new low-symmetry emerging materials that may be used as energy harvesters because of their piezoelectric or ferroelectric properties. Among these, ferroelectric metal-free perovskites are a class of recently discovered multifunctional materials. The doped nanofibers, which are very flexible and have a high Young modulus, behave as active piezoelectric energy harvesting sources that produce a piezoelectric voltage coefficient up to g_{eff} = 3.6 VmN^{-1} and show a blue intense luminescence band at 325 nm. In this work, the pyroelectric coefficient is reported for the MDABCO-NH_4I_3 perovskite inserted in electrospun fibers. At the ferroelectric–paraelectric phase transition, the embedded nanocrystals display a pyroelectric coefficient as high as 194 × 10^{-6} $Cm^{-2}k^{-1}$, within the same order of magnitude as that reported for the state-of-the-art bulk ferroelectric triglycine sulfate (TGS). The perovskite nanocrystals embedded into the polymer fibers remain stable in their piezoelectric output response, and no degradation is caused by oxidation, making the piezoelectric perovskite nanofibers suitable to be used as flexible energy harvesters.

Keywords:

organic lead-free perovskites; piezoelectric crystals; nanofiber composites; electrospinning; blue luminescence; functional organic materials

1. Introduction

diffraction peak above the background. The Lorentzian and Gaussian functions are:

$$L(x) = \frac{\left(2/\pi\beta^*\right)}{1+4x^2}$$
$$G(x) = \frac{2}{\beta^*}\sqrt{\frac{\ln(2)}{\pi}}\exp(-4\ln(2)x^2) \qquad (2a)$$

written in terms of the scaled diffraction angle

$$x = \frac{2\left(2\theta - 2\theta_c\right)}{\beta^*} \qquad (2b)$$

and the asymmetric width function [3]

$$\beta^* = \frac{2\beta}{1+\exp\left[a\left(2\theta - 2\theta_c\right)\right]} \qquad (2c)$$

In these expressions, the calculated peak position is $2\theta_c$ and a represents the asymmetry parameter.

The resulting fits are shown in Figure S1 a) to) while Tables S1 and S2 list the fit parameter values $(A,\eta,\theta_c,\beta,a)$ for the two peaks $(11\bar{1})$ and (200). The red shading in Figure S1 represents the 68% confidence intervals of the fit peaks.

Table S1: Fit parameter values for the MDABCO-NH_4I_3 embedded into PVC, PA66 and PMMA correspondent to Bragg reflection $(11\bar{1})$.

	A	η	$2\theta_c$	β	a
MDABCO-NH_4I_3@ PVC	9.02	1.00	21.947º	0.124º	-6.35
MDABCO-NH_4I_3@ PA66	12.639	1.00	21.941º	0.099º	-2.45
MDABCO-NH_4I_3@ PMMA	19.50	1.00	21.883	0.100º	4.846

Table S2: Fit parameter values for the MDABCO-NH_4I_3 embedded into PVC, PA66 and PMMA correspondent to Bragg reflection (200).

	A	η	$2\theta_c$	β	a
MDABCO-NH_4I_3@ PVC	12.84	0.60	24.676º	0.158º	16.51
MDABCO-NH_4I_3@ PA66	9.07	1.00	24.702º	0.103º	6.37
MDABCO-NH_4I_3@ PMMA	14.10	0.65	24.649º	0.121º	3.53

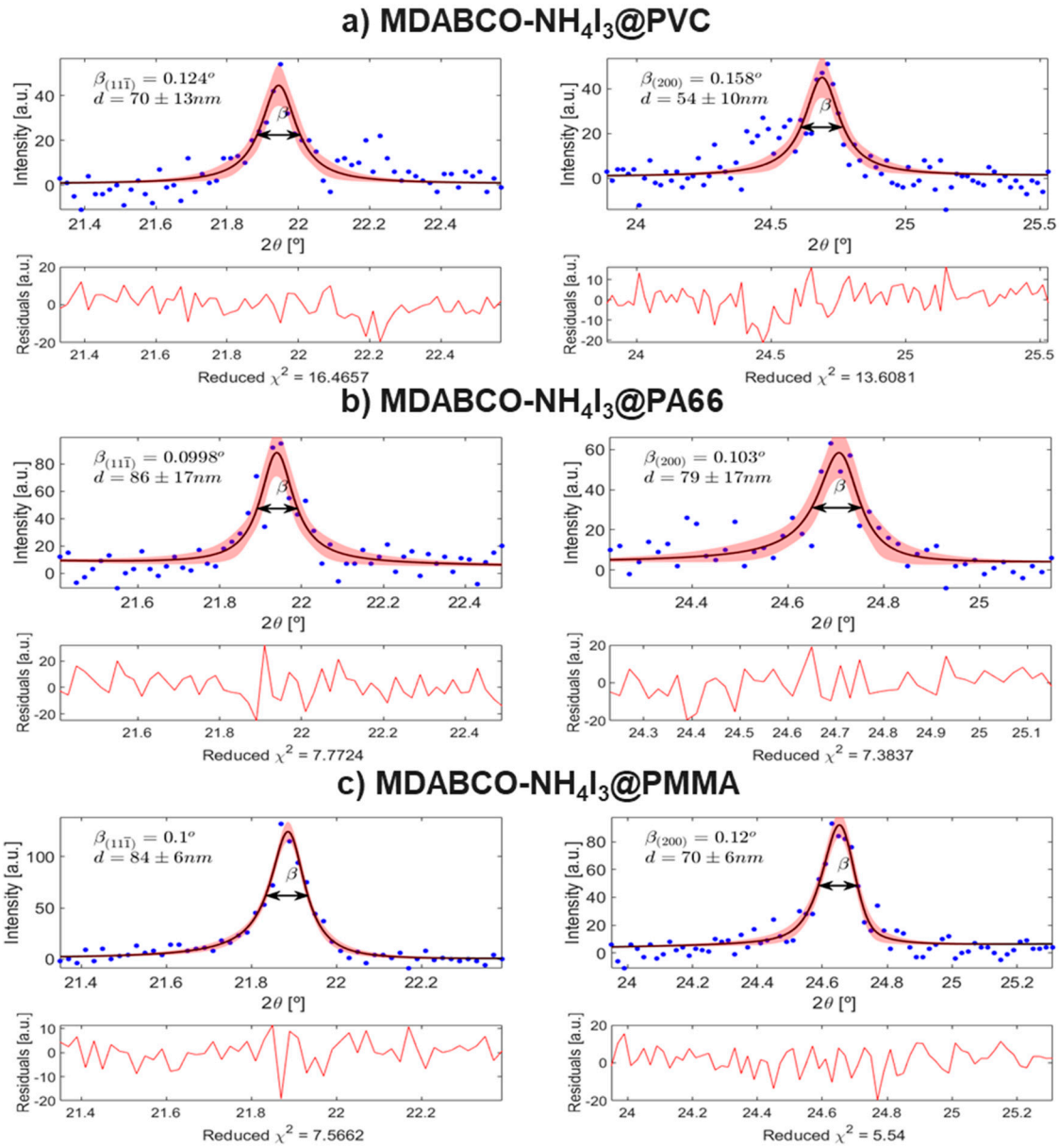

Figure S1. Asymmetric Pseudo-Voigt fits of the (11$\bar{1}$) and (200) Bragg reflections for MDABCO-NH_4I_3 crystals inside a) PVC, b) PA66 and c) PMMA nanofibers. The width of the reflections at half the maximum β and the nanocrystals average size d is indicated as well the refit residuals.

S2. UV-Visible Reflectance Spectra

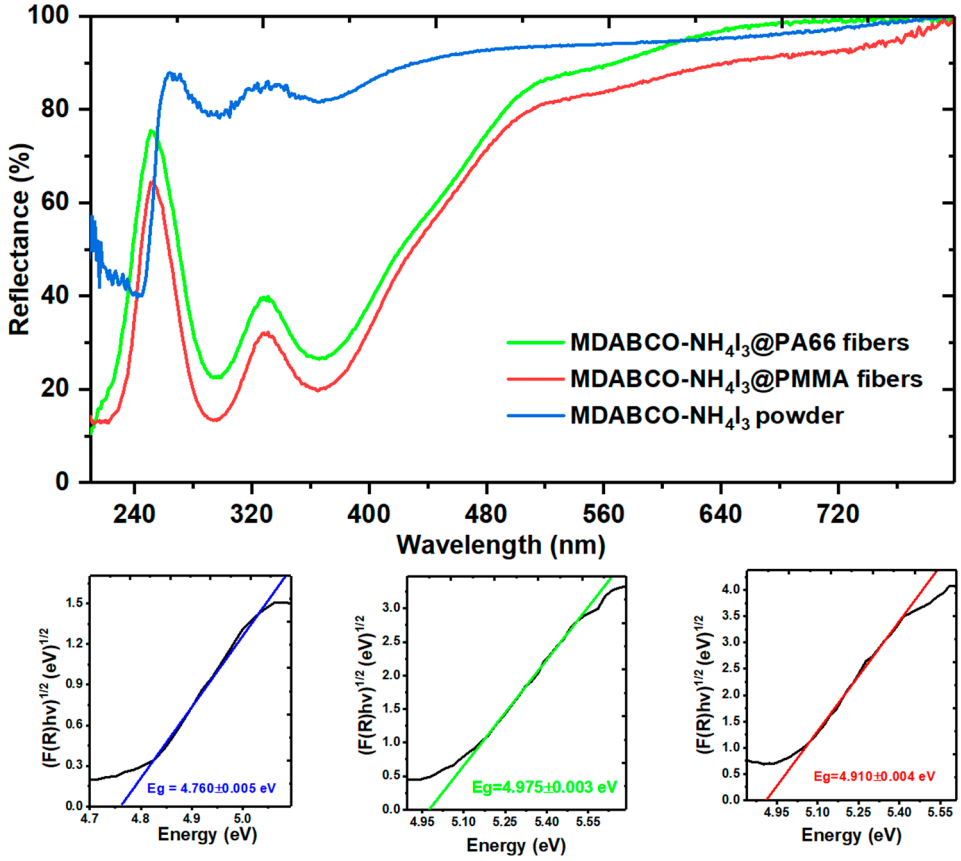

Figure S2. UV–vis reflectance of MDABCO-NH_4I_3 powder pellet and electrospun fibers. The inset shows the Kubelka-Munk function indicating a band gap energy of 4.760 eV for the polycrystalline perovskite, 4.975 eV and 4.910 eV for MDABCO-NH_4I_3@PA66 and MDABCO-NH_4I_3@PMMA nanofibers, respectively.

S3. DSC analysis

In figure S3, the measured DSC of synthesized MDABCO-NH_4I_3 perovskite crystals, showed the ferroelectric-paraelectric phase transition to occur at 443 K with area 19.9 J/g. MDABCO-NH_4I_3 perovskite crystals start to decompose above 460 K with the formation of NH_4IO_3. Cooling down from 473 K, shows a peak at 350 K, area -13.26 J/g. During the second heating, a peak with maximum at 358 K and area 12.3 J/g is observed. These two peaks correspond respectively to the paraelectric to ferroelectric and ferroelectric-paraelectric phase transitions of

NH_4IO_3 compound, which was formed after the first heating [4]. The perovskite phase transition at 443 K is not recovered, which reveals that crystal thermal degradation starts above 460 K[5].

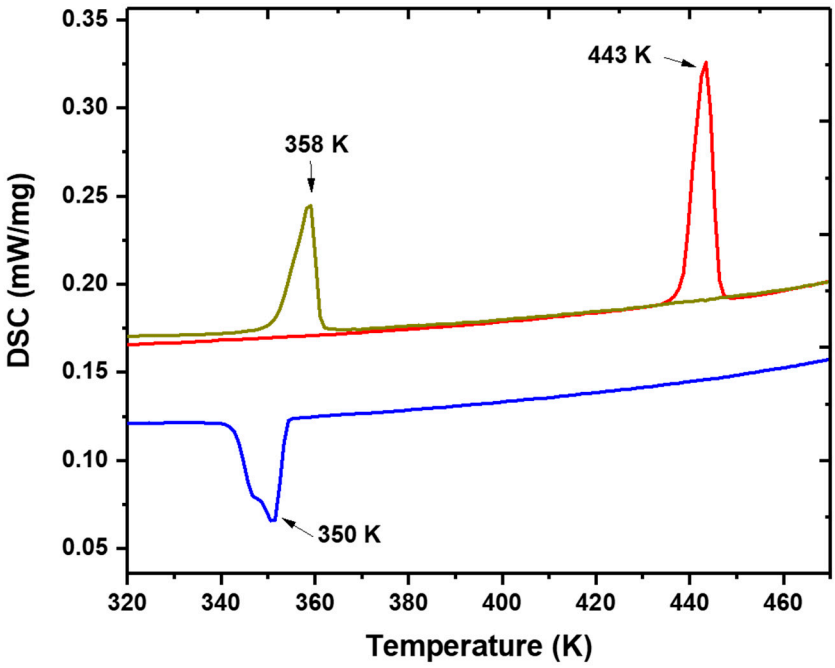

Figure S3. DSC spectra of synthesized MDABCO-NH_4I_3 perovskite crystals.

S4. RAMAN Spectra

In Figure S4, the measured Raman modes between $50 - 600\ cm^{-1}$ are shown for a MDABCO-NH_4I_3 polycrystalline sample, for electrospun fibers of PVC and MDABCO-NH_4I_3@PVC. In the spectra, the low frequency modes are due to lattice vibrations. From the two bands at $68\ cm^{-1}$ and $103\ cm^{-1}$ present in the polycrystalline sample, only the second band (now shifted to $109\ cm^{-1}$) remains intense for the perovskite nanocrystals embedded in the polymer fibers. The strong decreasing in intensity of the $68\ cm^{-1}$ band is probably the result of constrains imposed by the polymer matrix on the lattice vibrations modes, due to crystal confinement.

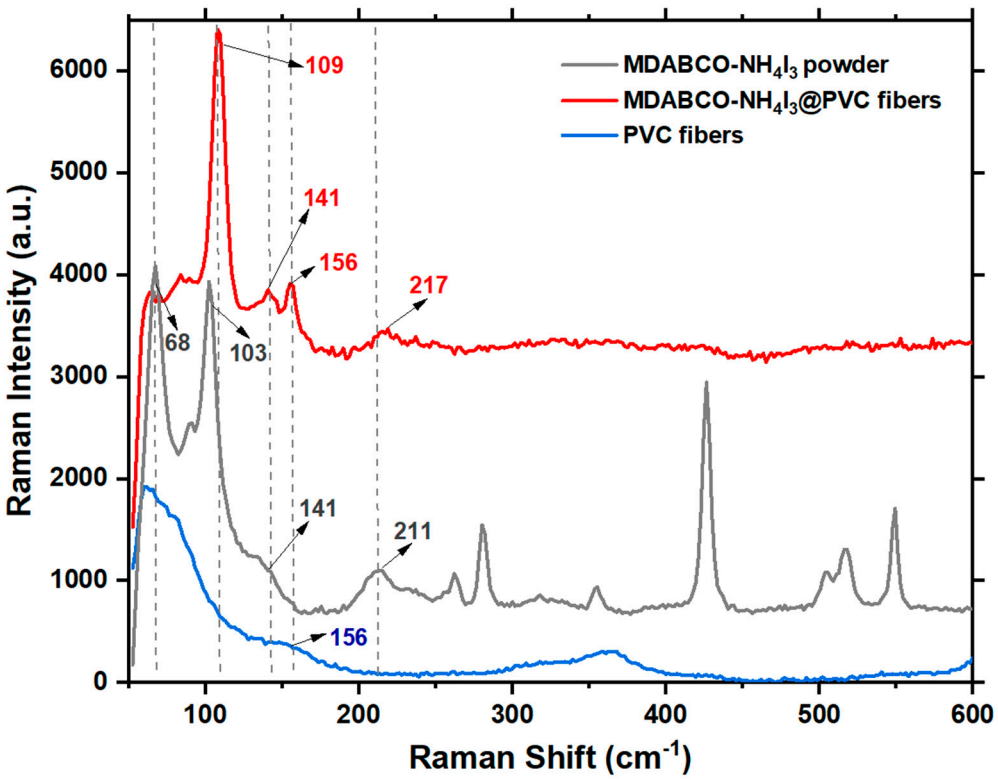

Figure S4. Raman spectra for MDABCO-NH_4I_3 polycrystalline sample (black line), for electrospun fibers of PVC (blue line) and MDABCO-NH_4I_3@PVC fibers (red line), expansion between $50 - 600\ cm^{-1}$.

The weak broad bands centred at 141 cm^{-1} for polycrystalline MDABCO-NH_4I_3 and 156 cm^{-1} for PVC fibers, are resolved into well-defined bands for MDABCO-NH_4I_3@PVC fibers. The weak band for MDABCO-NH_4I_3 at 211 cm^{-1} is slightly shifted to 217 cm^{-1}, for the perovskite incorporated into the fibers.

Noticed that for MDABCO-NH_4I_3@PVC fibers, none of the Raman peaks between $250 - 600\ cm^{-1}$ are perceptible, while they are present in the MDABCO-NH_4I_3 perovskite spectra. We may conclude that the polymer matrix strongly constrains these perovskite vibrational modes as mentioned above, which is expectable as the fibers were electrospun from a precursor solution with ration of MDABCO-NH_4I_3 to PVC of 1:5.

S5. FTIR-ATR analysis

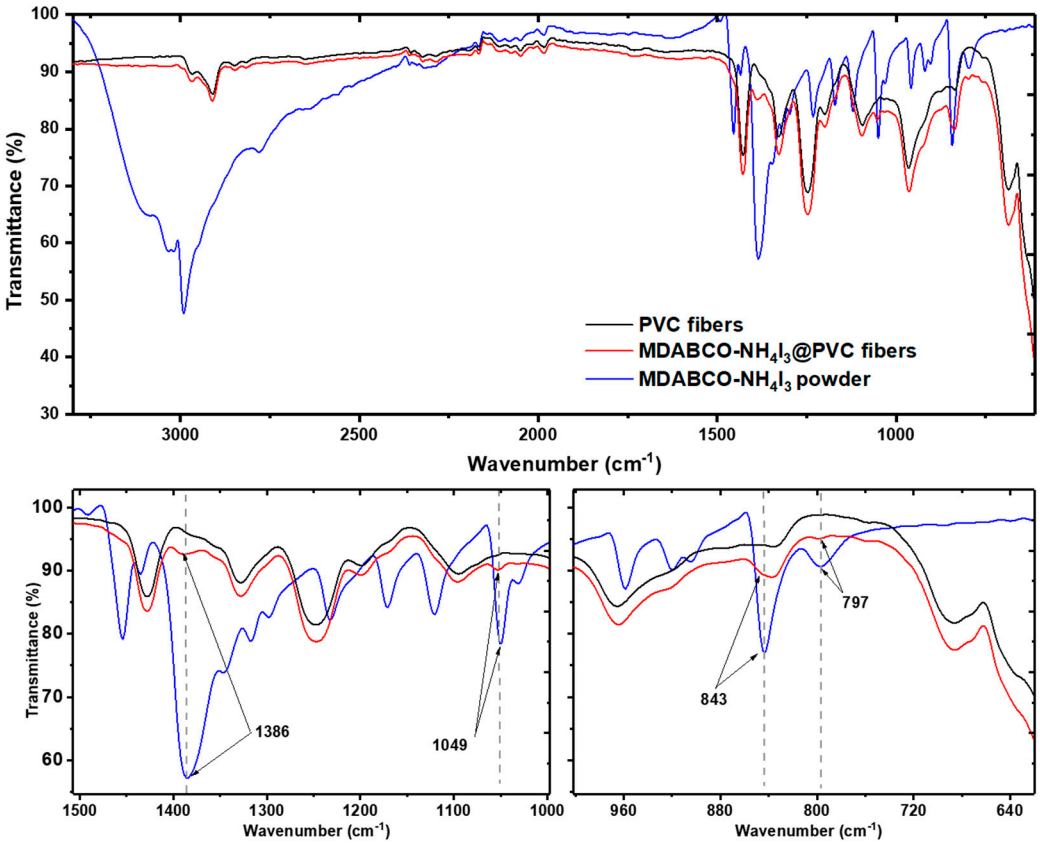

Figure S5. FTIR-ATR spectra of PVC polymer, MDABCO-NH_4I_3 powder and MDABCO-NH_4I_3@PVC fibers, a) full measurement and b) expansion between $1000 - 1500\ cm^{-1}$ and $600 - 1000\ cm^{-1}$.

In Figure S5 b), the measured FTIR-ATR between $1500 - 600\ cm^{-1}$ is shown for a MDABCO-NH_4I_3 polycrystalline sample, for electrospun fibers of PVC and MDABCO-NH_4I_3@PVC. Slight differences were observed between the spectra of electrospun fibers of PVC and MDABCO-NH_4I_3@PVC, and just few bands (the most intense) were possible to be assigned to MDABCO-NH_4I_3 perovskite nanocrystals at the 1386 cm^{-1}, 1049 cm^{-1}, 843 cm^{-1} and 797 cm^{-1}. However, the strong decreasing in intensity observed for the perovskite bands on electrospun fibers of MDABCO-NH_4I_3@PVC sample is due to the sobreposition of the polymer bands to those of MDABCO-NH_4I_3 crystals. As already mentioned, the ratio perovskite and polymer are 1:5, on the precursor solution used to fabricate

the electrospun fibers. Therefore, is expected that the only the stronger perovskite bands will be observed. That contained a concentration constrain imposed by the polymer matrix on the IR bands.

S6. Piezoelectric nanogenerator

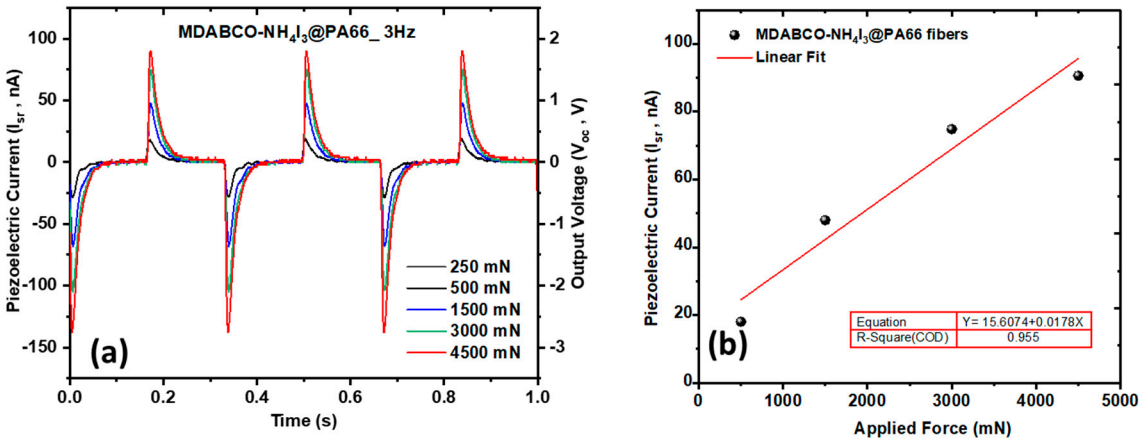

Figure S6. MDABCO-NH_4I_3@PA66 fibers (a) Piezoelectric current as function of time, for several applied forces and (b) linear fitting.

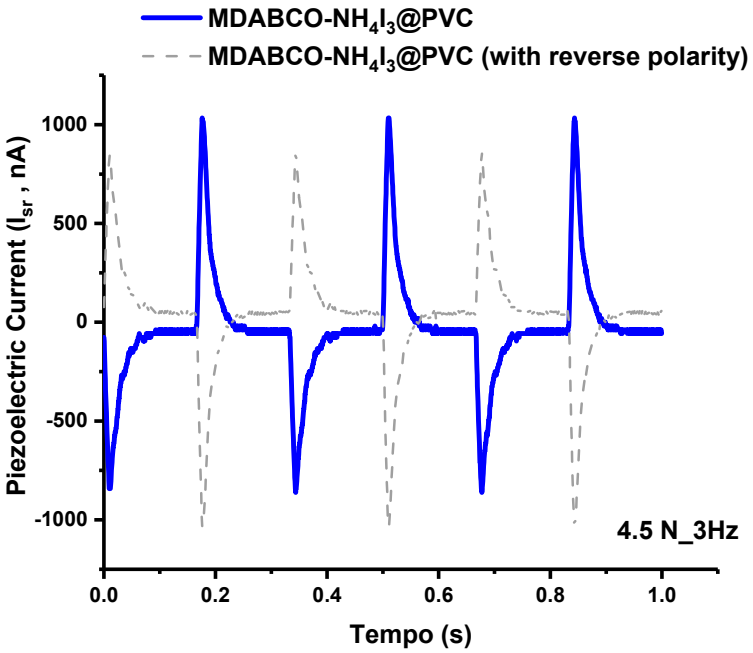

Figure S7. Output voltage generated from MDABCO-NH_4I_3@PVC nanofiber mat with reverse polarity.

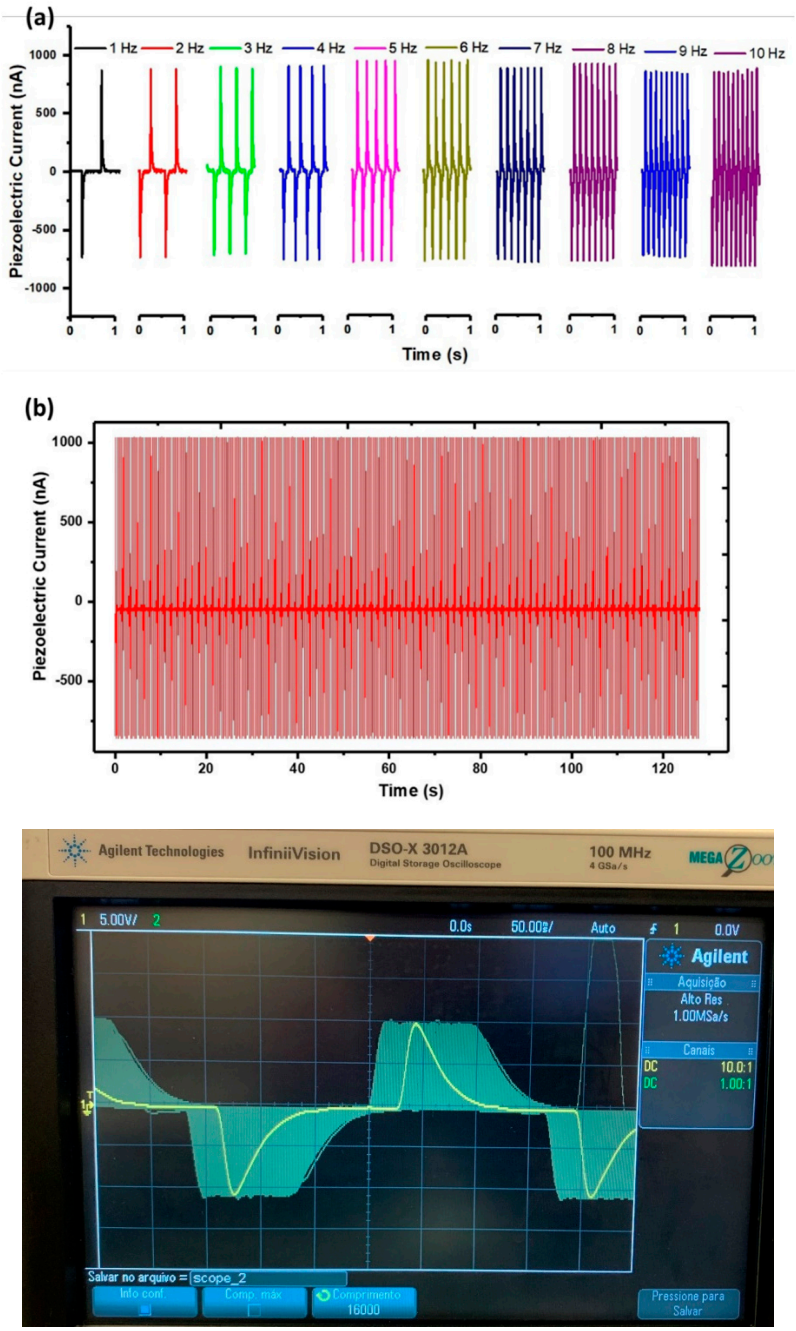

Figure S8. MDABCO-NH_4I_3@PVC nanofiber mat piezoelectric current generated a) for frequencies between 1Hz and 10 Hz and b) a 130 s interval under a periodical force applied with 4.5 N. A stability test was performed during a time interval of 4 h under a periodical force applied with 2.7 N at a frequency of 3 Hz (oscilloscope image).

S9. Mechanical Properties

Tensile strain applied to PVC and MDABCO-NH_4I_3@PVC electrospun fiber mat are shown in Figure S9. The results from tensile measurements show that MDABCO-NH_4I_3@PVC fibers exhibit good mechanical performance with an average increase of 14% on tensile strength (reaching ~ 4.0 MPa) and an increase of 40% on the strength at yield reaching (~ 2.5 MPa) when compared with PVC fibers. More importantly, the Young modulus increases from ~20 MPa in PVC fibers to ~58 MPa in MDABCO-NH_4I_3@PVC fibers, an increase of around 66%. This significant increase of the Young modulus of perovskite doped electrospun fibers indicates that composite MDABCO-NH_4I_3@PVC are mechanically stronger than neat polymer fibers. This is very important for the performance of MDABCO-NH_4I_3@PVC fiber mat as nanogenerator as it will increase its capability of supporting longer times under applied external force.

The decrease of 30% on the strain at break for doped fibers indicates a decrease in their plasticity, which might result from the presence of nanocrystals inside the PVC polymer which inhibits the capability for the PVC chains to flow between.[6]

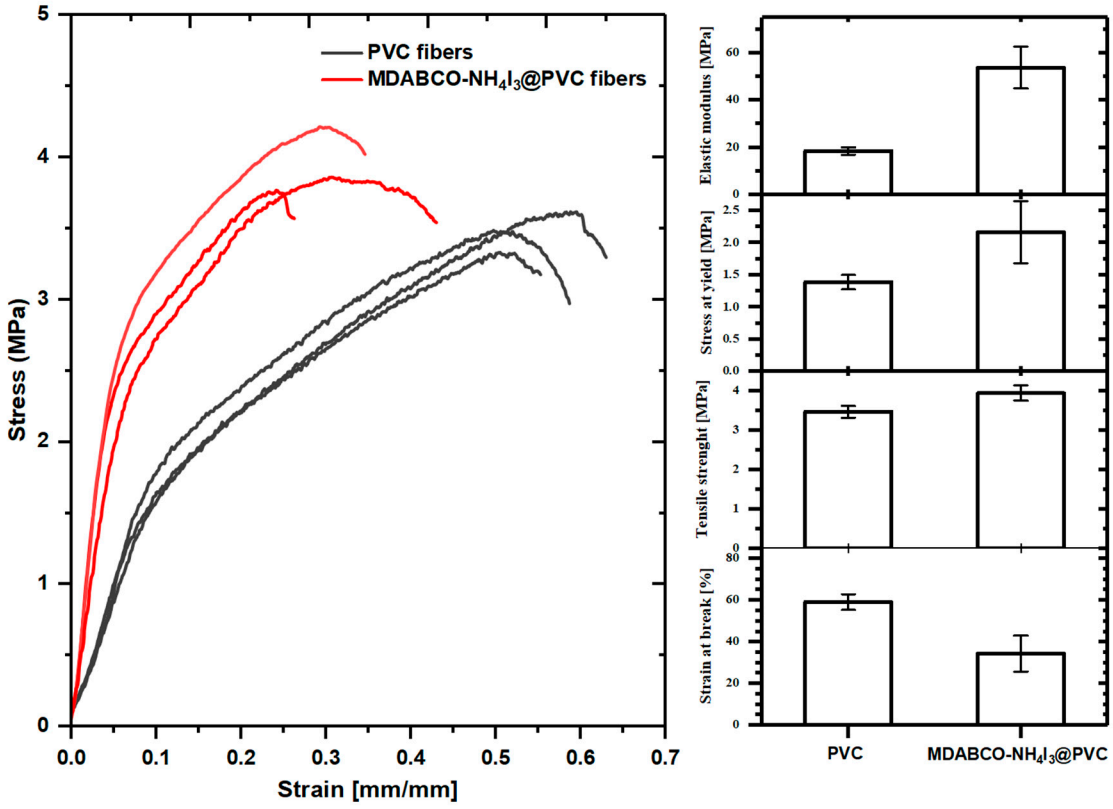

Figure S9. Elastic modulus, stress at yield, tensile strength and strain at break of PVC and MDABCO-NH_4I_3@PVC electrospun fibers.

References

(1) Klug, H.; Alexander, L., *X-Ray Diffraction Procedures 2nd edn*, Ch. 9. Wiley: 1974.

(2) John D'Errico (2022). SLM - Shape Language Modeling. https://www.mathworks.com/matlabcentral/fileexchange/24443-slm-shape-language-modeling), MATLAB Central File Exchange. Retrieved July 5, 2022.

(3) Stancik, A. L.; Brauns, E. B. A simple asymmetric lineshape for fitting infrared absorption spectra. *Vib Spectrosc* **2008,** *47* (1), 66-69, DOI: https://doi.org/10.1016/j.vibspec.2008.02.009.

(4) Keve, E. T.; Abrahams, S. C.; Bernstein, J. L. Pyroelectric Ammonium Iodate, a Potential Ferroelastic: Crystal Structure. *The Journal of Chemical Physics* **1971,** *54* (6), 2556-2563, https://doi.org/10.1063/1.1675212.

(5) Sirbu, D.; Tsui, H. C. L.; Alsaif, N.; Iglesias-Porras, S.; Zhang, Y.; Wang, M.; Liu, M.; Peacock, A. C.; Docampo, P.; Healy, N. Wide-Band-Gap Metal-Free Perovskite for Third-Order Nonlinear Optics. *Acs Photonics* **2021,** *8* (8), 2450-2458, https://doi.org/10.1021/acsphotonics.1c00687.

(6) Lee, D. W.; De Los Santos V, L.; Seo, J. W.; Felix, L. L.; Bustamante D, A.; Cole, J. M.; Barnes, C. H. W. The Structure of Graphite Oxide: Investigation of Its Surface Chemical Groups. *The Journal of Physical Chemistry B* **2010,** *114* (17), 5723-5728, https://doi.org/10.1021/jp1002275.

Mechanical energy harvesting at low frequencies from materials that are environmentally friendly and scavenging energy from multiple sources, for example, human body movements, are at the forefront of research [**1**,**2**].

Ferroelectrics are inherently piezoelectric and pyroelectric materials; that is, they are able to produce an intrinsic electrical potential difference in response to an applied force (or originate a mechanical movement due to an applied electric field) and a temperature gradient, respectively.

Valasek discovered the first ferroelectric, Rochelle salt or potassium sodium tartrate tetrahydrate [$KNaC_4H_4O_6$] ($4H_2O$) in 1920 and was, in fact, the first semiorganic molecular ferroelectric crystal that is also nontoxic [**3**,**4**].

Among ferroelectrics, the inorganic perovskites (formula ABX_3 (A, B = metal cations, X = anion; usually an oxide)) are a well-known family of solid-state inorganic compounds finding application in capacitors, sensors, actuators, etc. The best known are metal oxides such as strontium, barium, or lead titanate ($SrTiO_3$, $BaTiO_3$, $PbTiO_3$, respectively), and their solid solutions such as $Pb(Zr,Ti)O_3$ (PZT), niobates such as PZN ($PbZn_{1/3}Nb_{2/3}O_3$) (PZN), ($PbMg_{1/3}Nb_{2/3}O_3$) (PMN), and lithium niobate $LiNbO_3$). These materials have, until now, been used by several industries largely because of their functional properties, their combining ferroelectricity with nonlinear optical and electro-optic effects, as well as their multiferroicity [**5**,**6**].

So far, the commercially available piezoelectrics are dominated by inorganic perovskites, namely PZT-based materials, and polymers such as polyvinylidene difluoride (PVDF) and its modifications such as PVDF-TrF [**7**,**8**]. However, because of lead toxicity, lead-based ferroelectrics are presently a serious environmental hazard. These concerns originated active research on substituting those perovskite-type materials, one ion A or X, with a molecular building unit [**9**,**10**].

Hybrid organic–inorganic perovskites (HOIPs) are a recent class of ferroelectric crystalline materials for optoelectronic applications, which are competitive with inorganic perovskites. These semiorganic ferroelectrics possess many advantages when compared with inorganic ones. For example, they can be synthesized at room temperature, they are more flexible and with lower weight than their inorganic counterparts, and they have remarkable structural variability resulting in high tunable properties. Therefore, they became an attractive research topic for their application as piezoelectric and pyroelectric materials that replace inorganic materials [**11**,**12**,**13**,**14**]. Importantly, highly efficient solar cells have been demonstrated using methylammonium lead halide perovskites, which enabled the search for lead-free perovskites. Lead-free HOIPs are a recently discovered and highly promising family of perovskites [**15**,**16**,**17**,**18**,**19**,**20**].

A lead-free organic–inorganic perovskite recently discovered is (N-methyl-N'-diazabicyclo[2.2.2]octonium)–ammonium triiodide (MDABCO-NH_4I_3), which has a spontaneous polarization of 22 μC/cm^2, close to that of barium titanate (which is around 26 μC/cm^2), a high phase transition temperature at 448 K, and several polarization directions. It displays attractive properties for applications in flexible optoelectronic devices [**21**,**22**].

The fabrication of structures at the nanoscale has been attracting an increased amount of attention because of their size-dependent properties. One-dimensional structures such as nanowires, nanotubes, and nanofibers are the smallest dimensional structures displaying new properties with potential applications in fields such as electronics, photonics, sensing, and energy harvesting.

Electrospinning is a well-established technique for forming micro- and nanoscale fibers with a large surface-to-volume ratio forming mats of several square centimeters area. Electrospun fiber mats are nanostructured multifunctional materials drawn from a precursor polymeric solution blended with functional nanoparticles under very strong static electric fields [**23**,**24**,**25**,**26**,**27**].

In addition, the nanofiber's anisotropic shape and large surface area ratio contribute to an increase in their mechanical strength and flexibility. In this context, nanoscale ferroelectrics with perovskite structure is a promising research area [**11**,**28**].

One application of functional electrospun fibers is in the harvesting of electrical nanoenergy at low frequencies through the piezoelectric effect because of the polarization induced by the material deformation [**29**]. Piezoelectric nanogenerators, usually called PENGs, show potential for powering low-power devices. An example of the use of a semiorganic perovskite as a PENG was reported for the methylammonium lead iodide ($CH_3NH_3PbI_3$) incorporated in PVDF polymer fibers made by electrospinning; an output voltage of approximately 220 mV at 4 Hz, under an applied force of approximately 7.5 N, a maximum output power of 0.8 mW/m^2 was generated [**30**].

In this manuscript, MDABCO-NH_4I_3 perovskite embedded into electrospun nanofibers is capable of acting as lead-free piezoelectric (PENG) nanogenerators for effective mechanical energy harvesting. In particular, for poly(vinyl chloride) (PVC) polymer, an instantaneous output power density of 2020 μWm^{-2} is delivered under the application of a mechanical periodical force. The pyroelectric coefficient of a polycrystalline MDABCO-NH_4I_3 in electrospun fibers has a similar order of magnitude to that displayed by hybrid ferroelectric triglycine sulfate (TGS).

2. Experimental Section

2.1. Materials and Nanofibers Preparation

MDABCO-NH_4I_3 was synthesized following the synthetic procedure reported by Yu-Meng You and Ren-Gen Xiong [**21**]. The precursor (MDABCO)I was synthesized, as reported by Kreuer et al. [**31**]. The MDABCO-NH_4I_3 crystals grown were ground in a mortar and sieved to a size smaller than 40 µm.

All chemicals and solvents were purchased from Sigma-Aldrich (Schenlldorf, Germany) and used as received. Poly (methyl methacrylate) (PMMA, Mw 120,000) was purchased from Alpha-Aesar (Kandel, Germany). Polyamide 66 (PA66) and Poly(vinyl chloride) (PVC), high molecular weight, a density of 1.40 g/mL), were purchased from BDH Chemicals (Poole, UK) and Janssen (Beerse, Belgium), respectively. The 10% polymer solution (*w*/*v*) of PMMA was prepared by dissolving the powder in a dichloromethane (DCM)/*N*,*N*-dimethylformamide (DMF) solvent blend system (80:20, *v*/*v*), with vigorous stirring (400–600 rpm) at room temperature. The 10% (*w*/*v*) of polymer solution of PA66 was prepared by dissolving the polymer in 5 mL of 1,1,1,3,3,3-hexafluoro-2-propanol (HFP) with vigorous stirring (400–600 rpm) at room temperature. Then, a 10% precursor electrospinning solution of PVC was prepared by dissolving the pellets in 5 mL of the tetrahydrofuran (THF)/DMF (50:50, *v*/*v*) solvent blend system. After complete dissolution, 0.1 g of MDABCO-NH_4I_3 was ground and incorporated in small portions in a 1:5 weight ratio, and the resulting solution was sonicated for 10 min and stirred for several hours under ambient conditions before the electrospinning process, shown in **Figure 1**.

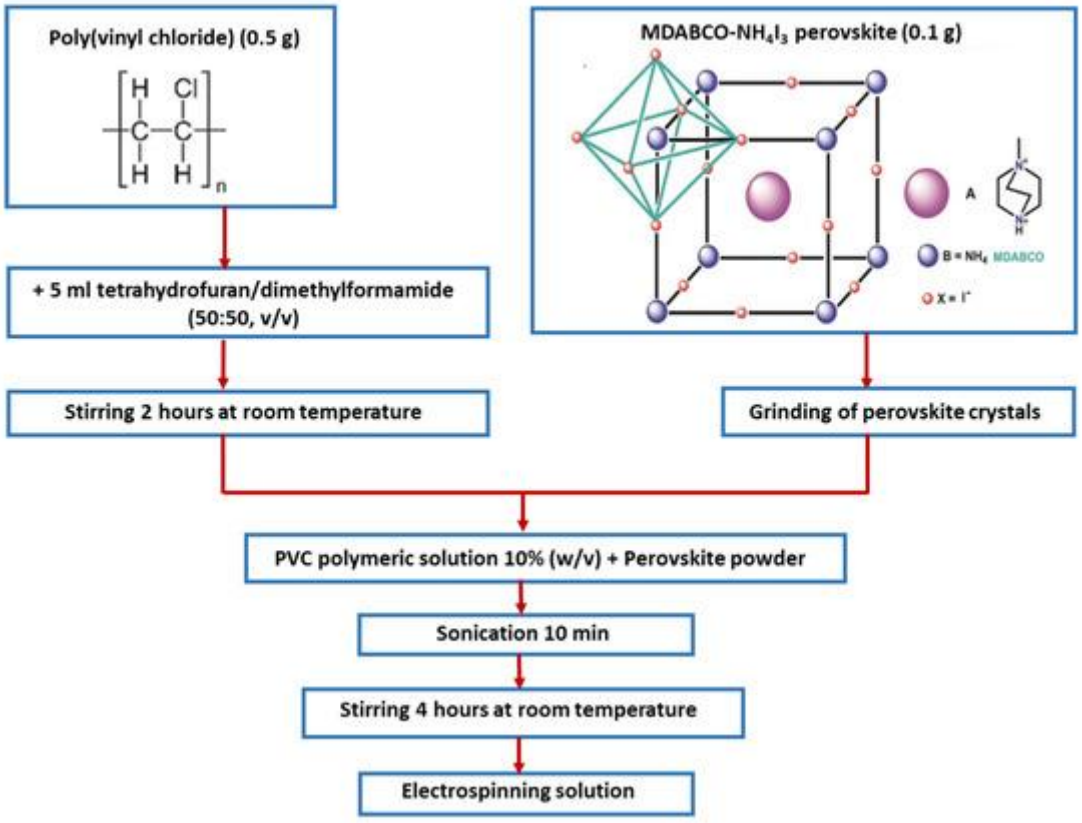

Figure 1. MDABCO-NH_4I_3 perovskite crystal flow chart for the preparation of MDABCO-NH_4I_3 @PVC electrospinning solution.

The precursor solution was loaded into a 5 mL syringe with its needle (0.5 mm outer diameter and 0.232 mm inner diameter) connected to the anode of a high-voltage power supply (Spellmann CZE2000, Bochum, Germany). The nanofibers were produced by a conventional electrospinning technique, previously described in [**26**,**32**], with a configuration that tends to produce oriented fiber mats. Briefly, the equipment used has four common components: a high-voltage power supply, a precision syringe pump, a syringe fitted with a metal needle (spinneret), and a drum collector (connected to a motor speed controller). The power supply is connected to both the spinneret and the drum collector. The polymer solution is extruded through the spinneret at a constant flow rate controlled by the syringe pump. An aluminum foil is attached to the collector in order to collect the prepared fibers. Our electrospinning apparatus has a vertical geometry.

Polymer nanofibers with embedded MDABCO-NH_4I_3 perovskite using three different polymers were fabricated. Solutions with pure PVC, PMMA, and PA66 polymers were also electrospun and taken as a reference. For the electrospinning of MDABCO-NH_4I_3 containing polymers and reference solutions, a voltage of 18 kV was applied between the tip and collector. The flow rate of the solution and the needle-to-collector distance were kept at 0.18–0.30 mL/h and 12 cm, respectively.

The MDABCO-NH_4I_3 crystals are not stable in the open air at room temperature. When the crystals are exposed to air, the perovskite oxidizes, as shown in **Figure 2**a,b. The iodide ions slowly oxidize. The product is molecular iodine, I_2, which darkens the crystals. Previously, to prepare precursor electrospinning solutions, several solvents were tested. In **Figure 2**c, it is possible to see that for solvents tetrahydrofuran (THF), methanol, ethanol, and acetone, the intense dark yellow color appears because of the degradation of the perovskite. Hexafluoroisopropanol (HFP) was chosen to prepare the electrospun polymer-doped solutions because the solutions remain stable, and the perovskite is protected from oxidation for long periods of time after preparation.

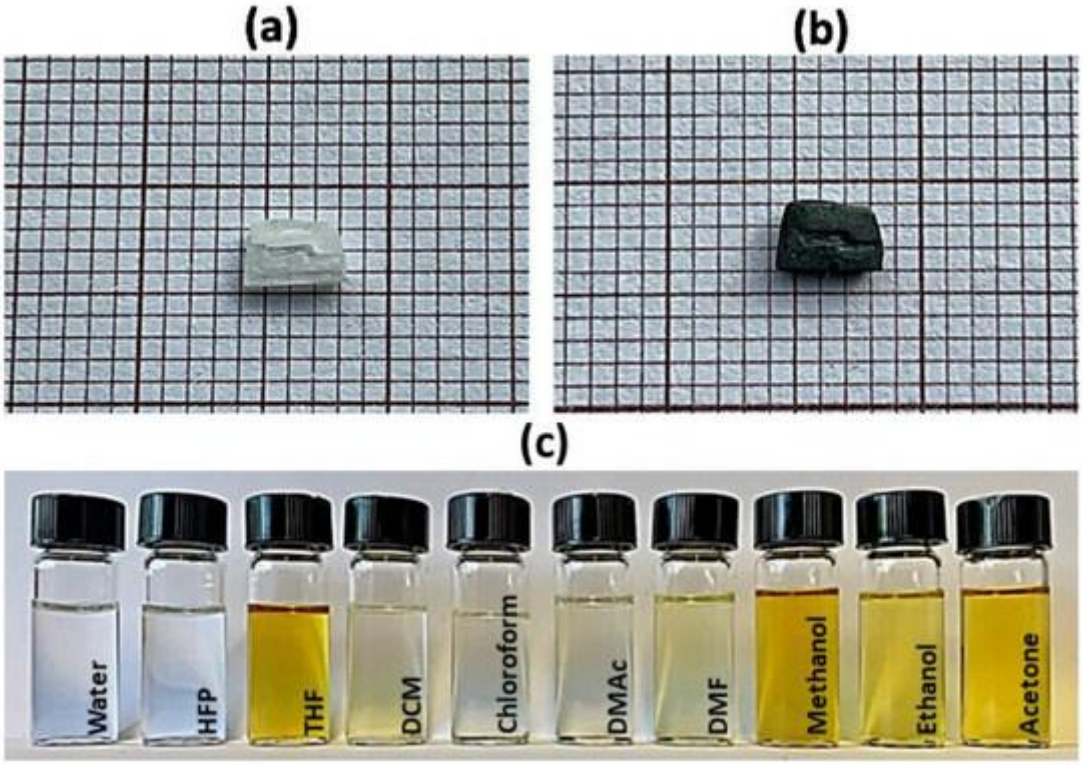

Figure 2. MDABCO-NH_4I_3 perovskite crystal, after several hours (**a**) and after 2 weeks (**b**) of exposure in the open air at room temperature. Perovskite solutions in different solvents (**c**), from left to right: water, hexafluoroisopropanol (HFP), tetrahydrofuran (THF), dichloromethane (DCM), chloroform, dimethylacetamide (DMAc), dimethylformamide (DMF), methanol, ethanol, and acetone.

To make good use of the outstanding crystal properties, we found that, by embedding them into a polymer matrix, the perovskite crystals are protected from oxidation while keeping their optical, piezoelectric, and pyroelectric properties. The perovskite nanocrystals, when embedded into the fibers, are stable for more than half a year because the polymers function as shields protecting the perovskites from oxidation.

PMMA was chosen to prepare the hybrid matrix with MDABCO-NH_4I_3 organic perovskite because it is a biocompatible polymer. PA66, a polymer with a high melting point at 275–280 °C, was also chosen because it enables the measurement of the pyroelectric effect on the perovskite nanofibers near their Curie temperature. Finally, PVC polymer was chosen because of its nontoxicity, flexibility, strength, and high melting point around 220 °C. The electrospinning process was stable for all the polymers chosen, and the obtained fibers showed uniform surfaces and small diameters, demonstrating that there were no crystallites on their surface. The hybrid functional MDABCO-NH_4I_3@PVC, MDABCO-NH_4I_3@PA66, and MDABCO-NH_4I_3@PMMA nanofibers were further utilized for optical and dielectric characterization, as well as the exemplification of a piezoelectric voltage generator.

2.2. Scanning Electron Microscopy (SEM)

The morphology, size, and shape of MDABCO-NH_4I_3 perovskite nanofibers were studied using a Nova Nano SEM 200 scanning electron microscope (FEI Company, Hillsboro, OR, USA), operated at an accelerating voltage of 10 kV. Nanofibers were deposited on a silica surface previously covered with a thin film (10 nm thickness) of Au-Pd (80–20 weight %) using a high-resolution sputter cover, 208HR Cressington Company (Watford, UK), coupled to a Cressigton MTM-20 high-resolution thickness controller. The diameter range of the nanofibers was measured by SEM images using ImageJ 1.51n image analysis software (ImageJ2, NIH, **https://imagej.nih.gov/ij/**, 12 September 2022). The average diameter and diameter distribution were determined by measuring 80 random nanofibers from the SEM images, and the fiber diameter distributions fit to a log-normal function.

2.3. X-ray Diffraction and Raman Spectroscopy

The crystallinity and crystallographic orientation of MDABCO-NH_4I_3 inside the fibers were studied by X-ray diffraction. The diffraction pattern using θ–2θ scans was recorded on a Bruker D8 Discover (Bruker company, Billerica, MA, USA) with Cu-Kα radiation of wavelength 1.5406 Å.

Raman spectroscopy was performed on a LabRAM HR Evolution confocal Raman spectrometer (Horiba Scientific, France, Lille) using Horiba Scientific's Labspec 6 Spectroscopy Suite software (LabSpec-Version 6) for instrument control, data acquisition, and processing. The Raman spectra were obtained using a laser excitation with wavelength 532 nm, at 0.1% laser intensity, with 30 s acquisition time in a spectral range between 50 and 3500 cm^{-1}.

2.4. Mechanical Tests

Elastic modulus, stress at yield (at 0.2% offset), tensile strength, and strain at break (at 60% tensile strength) were measured using a universal tensile testing machine Zwick/Roell Z005 (ZwickRoell, Germany), following the ASTM D882–02 standard. Several 10 × 30 mm samples, with a gauge length of 16 mm, were tested alongside the oriented fiber direction under a crosshead velocity of 25 mm/min.

2.5. Optical Absorption and Photoluminescence

Optical absorption (OA) measurements on an MDABCO-NH_4I_3 solution were carried out using a Shimadzu UV-3101PC UV–Vis-NIR (Shimadzu Corporation, Kyoto, Japan) spectrophotometer. Photoluminescence spectra were recorded on a Fluorolog 3 spectrofluorimeter (HORIBA Jobin Yvon IBH Ltd., Glasgow, UK). For optical absorption measurements, a 3 mg/mL solution of MDABCO-NH_4I_3 was prepared in water. The sample was measured in a quartz cuvette with a 1 cm path length.

Photoluminescence (PL) spectra were acquired using an excitation wavelength of 290 nm, with input and output slits fixed to provide a spectral resolution of 3 nm.

The same spectrophotometer equipped with an integrating sphere, Shimadzu ISR-240A (Shimadzu, Duisburg, Germany), and barium sulfate taken as reference, was used to measure the diffuse reflectance spectrum for the nanofiber array in the wavelength range of 250–800 nm with 1 nm step size. The energy of the band gap (E_g) was determined using the Kubelka–Munk function given by $[[hvF(R)]^{1/2}] = \alpha(hv - E_g)$, where hv represents the energy of the incident photon, E_g corresponds to the energy of the bad gap, and F(R) is called the Kubelka–Munk function directly determined from the total reflectance coefficient of the material (R) through the equation $F(R) = (1 - R)^2/2R$ [**33**,**34**].

2.6. Dielectric Spectroscopy

The dielectric properties of the electrospun fibers with embedded MDABCO-NH_4I_3 inclusions were characterized by impedance spectroscopy, at temperatures of 300–460 K and in the frequency range of 20 Hz–3 MHz. The complex permittivity, written as $\varepsilon = \varepsilon' - i\varepsilon''$, where ε and ε" are the real and imaginary parts, respectively, were calculated from the measured capacitance (C) and loss tangent (tan δ), using the equations:

$C = \varepsilon'\varepsilon_0(A/d)$ and $\tan\delta = \varepsilon''/\varepsilon'$

Here A is the electric contact area, and d is the fiber mat thickness. To perform the measurements, the samples formed a parallel plate capacitor and were included in an LCR network. To form the capacitor, the aluminum foil used as the substrate to collect the fiber mats was the bottom electrode, while the top electrode was the base of cylindrical metal contact, with approximately 10^{-2} m diameter. A Wayne Kerr 6440A (Wayne kerr Electronics, London, UK) precision component analyzer was used together with a dedicated computer and software to acquire the data. Shielded test leads were employed to avoid parasitic impedances due to connecting cables. Temperature-dependent measurements were performed at a rate of 2 °C/min, using a Polymer Labs PL706 PID controller (Polymer Labs, Los Angeles, CA, USA) and furnace.

Pyroelectricity results from the temperature dependence of spontaneous polarization. By changing the temperature, an electric field originating from changes in intrinsic dipoles is compensated by the surface layer of free charges. The rate of change in the spontaneous polarization $p = dP_s/dT$ is the pyroelectric coefficient. The change in polarization was detected by measuring the pyroelectric current $I = A(dPs/dT)(dT/dt)$ with a Keithley 617 electrometer (Keithley Instruments GmbH, Landsberg, Germany), where A is the electrode area and dT/dt is the rate of

temperature change. The measurements were performed in a capacitor geometry under short-circuit conditions.

2.7. Fabrication of an MDABCO-NH_4I_3@PVC Piezoelectric Nanogenerator

A piezoelectric nanogenerator, fabricated using an MDABCO-NH_4I_3@PVC electrospun fiber mat as the active piezoelectric component, is described in **Figure 3**. The top and bottom electrodes (area 40 × 40 mm^2) are high-purity copper thin plates. Thin copper wires were attached to the electrodes. The entire system was laminated with 1mm thick cork sheets to protect and facilitate the handling of the nanogenerator.

Figure 3. Schematic of MDABCO-NH_4I_3@PVC. (**a**) Electrospun nanofiber mat sandwiched between two copper electrodes. (**b**) Wires attached to the electrodes. (**c**) The complete laminated system with thin cork sheets.

3. Results and Discussion

3.1. Electrospun Fibers

The perovskite polymer solutions obtained remain stable with no color change for several weeks, shown in **Figure 4**a. The electrospinning process is stable, with no current fluctuations and a steady flow of the polymer solution at the tip of the needle. The fabricated fibers are very flexible (inset), show no 'beads' or crystallites grown on their surface, have a white appearance and are flexible, **Figure 4**b.

Figure 4. Perovskite polymeric solution (**a**) and MDABCO-NH_4I_3@PVC electrospun nanofiber mat (**b**) the inset shows a fiber mat folded around a cylindrical stick, demonstrating the flexibility of the fibers.

3.2. Fibers Morphology and Crystallinity

Figure 5 shows scanning electron microscopy (SEM) images of the fibers prepared with different polymers with embedded MDABCO-NH_4I_3 perovskite, along with the corresponding histograms of the diameter sizes. The diameter distributions are observed to follow a log-normal dependence, with average values from 200 to 605 nm.

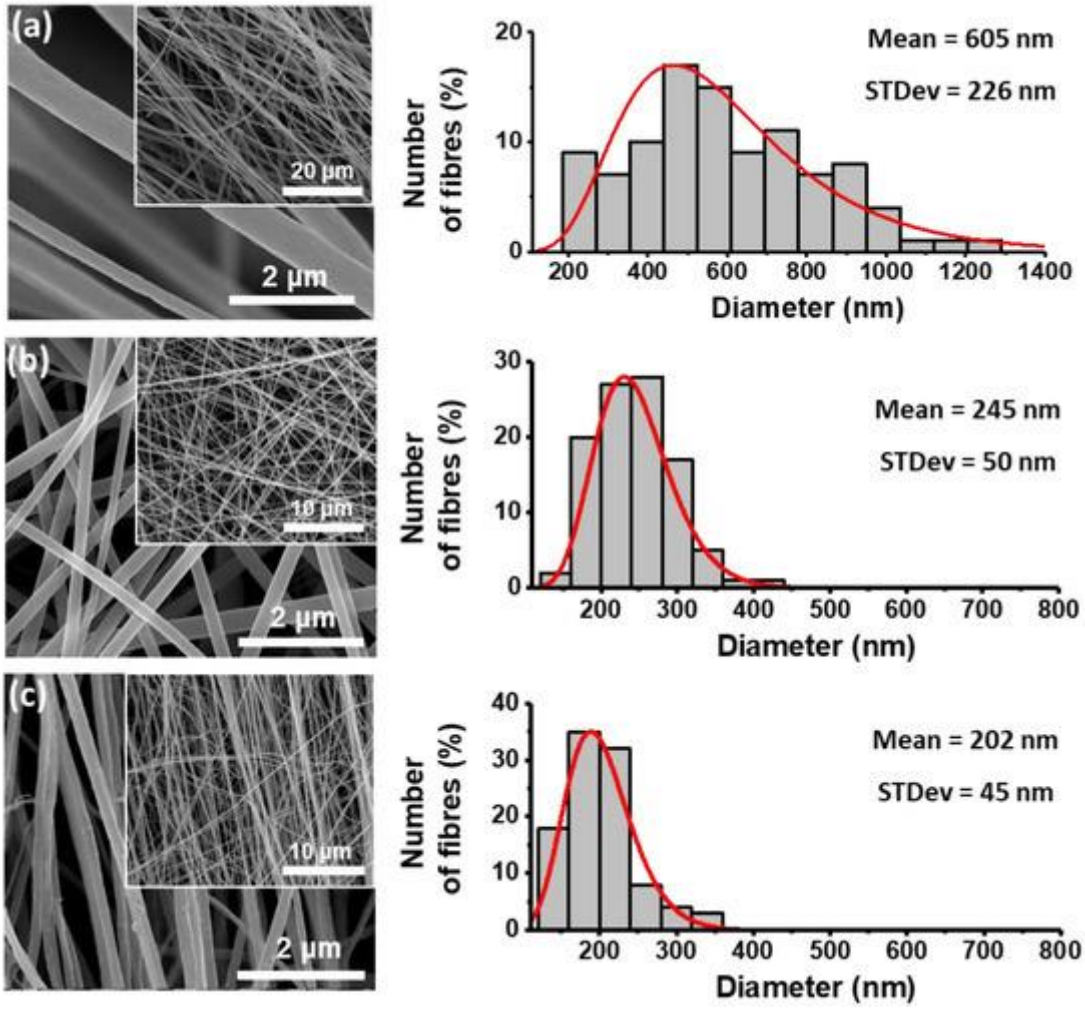

Figure 5. SEM images at magnification levels of 10,000× and 50,000× and respective fiber diameter distribution histograms for PMMA (**a**), PA66 (**b**), and PVC (**c**) nanofibers with embedded MDABCO-NH_4I_3 perovskite crystals. The red curves indicate logarithmic normal distributions using the mean and standard deviations of each set of fibers.

X-ray diffraction patterns obtained from the doped fibers are shown in **Figure 6**b–d and compared to the correspondent pattern for the polycrystalline synthesized MDABCO-NH_4I_3 perovskite, **Figure 6**a, where all the Bragg peaks were indexed using the published crystal structure (CIF file 1836322) [**21**]. We conclude that the embedded perovskite is in its crystalline ferroelectric phase for all fibers and is randomly oriented inside the different polymer matrices. The crystallite size of the perovskites was evaluated for each polymer, from fitting with the Debye–Scherrer

equation the two most intense Bragg reflections (111)111¯ and (200)200, see **SI, Figure S1a**–c. The average size varies between 62 and 83 nm, as indicated in **Table 1**.

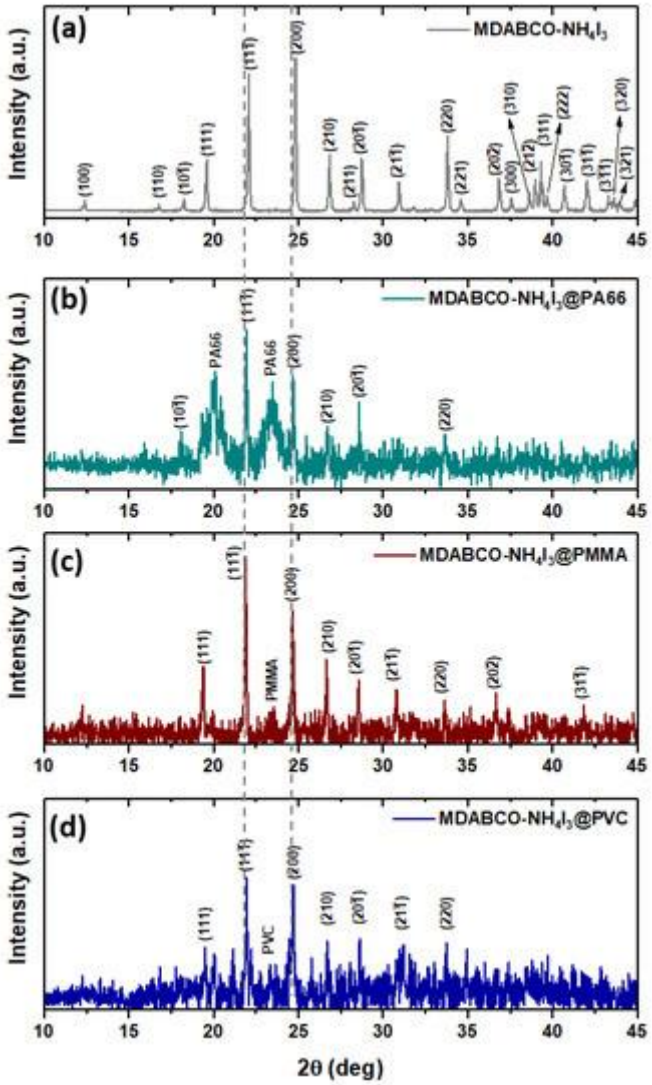

Figure 6. (**a**) Synthesized perovskite crystals with all Bragg peaks indexed from the published CIF file 1,836,322 [**17**]. X-ray patterns of PA66 (**b**), PMMA (**c**)**,** and PVC (**d**) nanofibers with embedded MDABCO-NH_4I_3 perovskite crystals between 10° and 45°.

Table 1. The average crystallite size of MDABCO-NH_4I_3 perovskite crystals embedded in electrospun fibers.

3.3. Optical Absorption and Luminescence

The reflectance spectra of an MDABCO-NH_4I_3 pellet and MDABCO-NH_4I_3@PVC nanofibers show two absorption bands with the maximum at wavelengths of 297 nm and 365 nm and 298 nm and 367 nm, respectively, as shown in **Figure 7**. PVC electrospun fibers are highly transparent in all UV–Vis spectra. The energy band gap, E_g, calculated for pellet crystals and nanofibers, from the intersection with the energy axis of a linear Kubelka–Munk function, are 4.760 eV and 4.824 eV, respectively, as indicated in the insets of **Figure 7**. These values are in excellent agreement with 4.950 eV, as previously reported in [**35**]. Similar reflectance spectra measured for MDABCO-NH_4I_3@PMMA and MDABCO-NH_4I_3@PA66 nanofibers are shown in **SI Figure S2**.

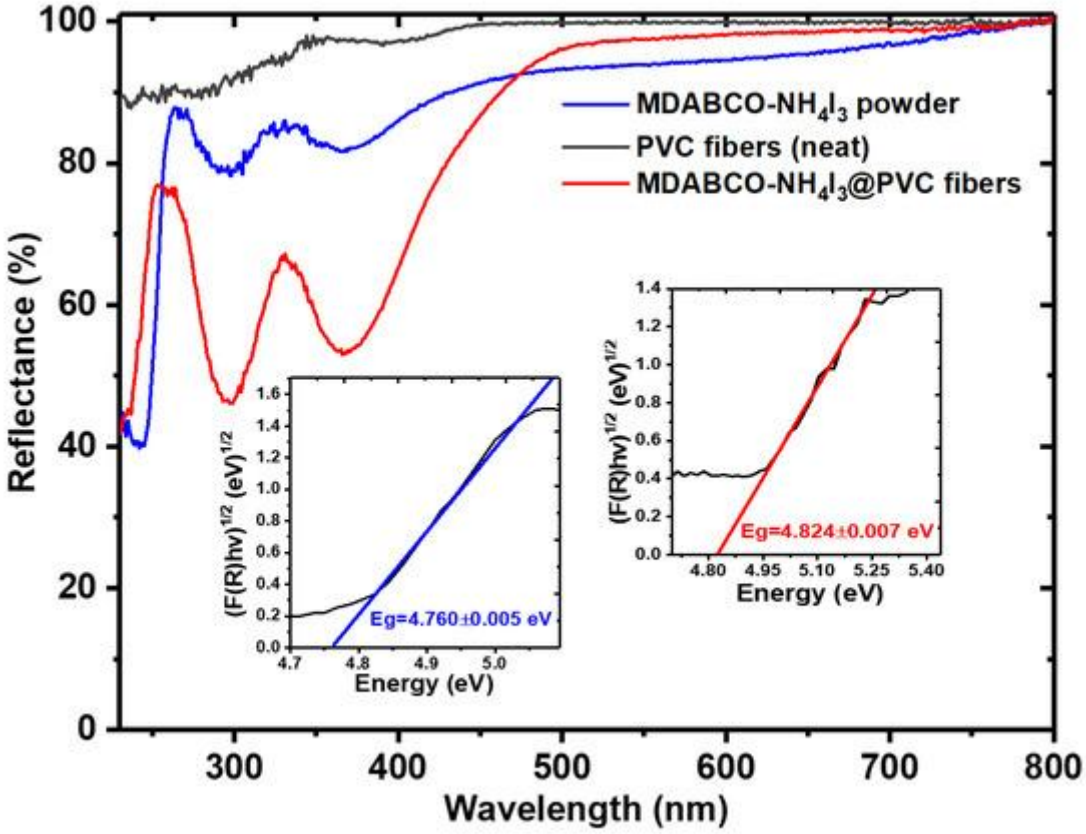

Figure 7. UV–vis reflectance of MDABCO-NH_4I_3 powder and electrospun PVC fibers with MDABCO-NH_4I_3 nanocrystals. The inset shows the Kubelka–Munk function indicating a band gap energy of 4.760 and 4.824 eV for powder and fibers, respectively.

At high wavelengths (low photon energies), both free perovskite and electrospun fibers containing the perovskite are highly transparent, and the absorption becomes stronger at the band-gap energy. High transparency in the visible and near-infrared regions of the optical spectra is important for linear and nonlinear optical applications [**36**,**37**].

Figure 8 shows the OA of a water solution MDABCO-NH_4I_3, the emission of PL from the same solution, and the dissolved MDABCO-NH_4I_3@PVC fibers for excitation at 289 nm. For the MDABCO-NH_4I_3 water solution, the PL emission shows one intense band in the UV with a maximum at 325 nm, a slightly lower intense band in the blue with a maximum at 395 nm, and a redshifted band with a maximum at 645 nm. For nanofibers (the solvent used dissolves only the polymer and not the perovskite nanocrystals), an extremely intense PL band at 325 nm and a less intense redshifted band with a maximum at 645 nm are observed. It is remarkable that MDABCO-NH_4I_3 nanocrystals inside the fibers show intense solid-state UV and blue luminescence, which is reported in this study for the first time for MDABCO-NH_4I_3 perovskite nanocrystals.

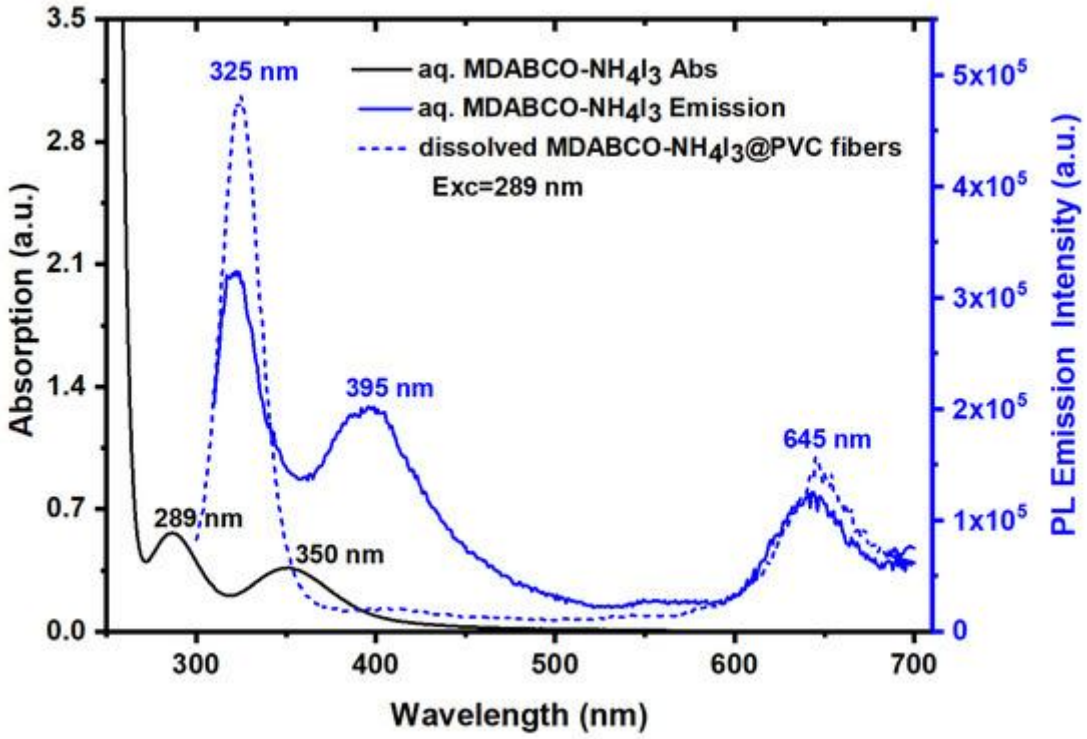

Figure 8. Optical absorption and photoluminescence emission of MDABCO-NH_4I_3 aqueous solution (3 mg/mL) and MDABCO-NH_4I_3@PVC nanofibers dissolved in tetrahydrofuran. The excitation wavelength for PL measurements were 289 nm.

3.4. Dielectric Measurements

The complex dielectric permittivity measured on a polycrystalline sample of MDABCO-NH_4I_3 (pellet), between 300 K and 470 K as a function of frequency, shows that the ferroelectric–paraelectric phase transition occurs at 440 K, shown in **Figure 9**a,b. As expected for a proper ferroelectric system, the real part of the permittivity increases with decreasing frequency, reaching the Curie transition temperature of 42,500 (at 20 Hz). Quite extraordinarily, this very high value of ε', measured on a pellet, is 3000 times higher than that reported for an oriented single crystal, which

was 14,068 at the same frequency of 20 Hz [**21**]. This indicates the high purity of our synthesized MDABCO-NH_4I_3 crystals.

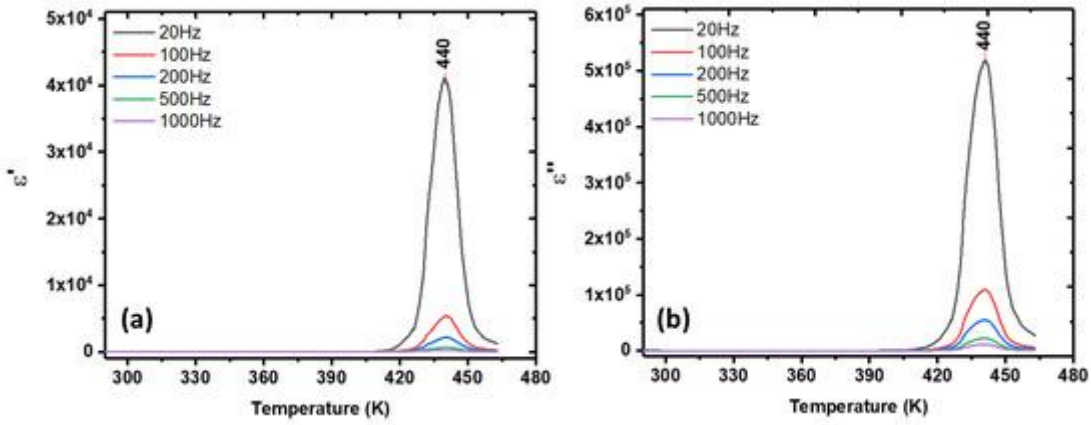

Figure 9. Dielectric permittivity of an MDABCO-NH_4I_3 polycrystalline sample showing its (**a**) real and (**b**) imaginary parts as functions of temperature and frequency. The ferroelectric–paraelectric phase transition occurs at 440 K.

The real and imaginary parts of the dielectric permittivity were also measured on an MDABCO-NH_4I_3@PA66 electrospun fiber mat in the same temperature and frequency range, as shown in **Figure 10** for frequencies below 1000 Hz. The transition is perceptible at 462 K, a little above the temperature of 440 K measured for a polycrystalline perovskite (**Figure 9**). When ferroelectric nanostructures are under stress/strain, their ferroelectric transition temperature varies compared with bulk unstressed ones. The shift in transition temperature depends on the strain state of the crystal. For example, hydrostatic strain tends to decrease the transition temperature [**38**], while anisotropic strain states can strongly increase the transition temperature [**39**,**40**]. In our case, from the X-ray diffraction results of **Figure 6**, we observe a slight shift of the XRD peaks compared with the bulk, indicating the MDABCO-NH_4I_3 nanocrystals are under strain inside the fibers. This nanofiber-induced strain is anisotropic because of the high aspect ratio of the nanofibers and has increased the transition temperature compared with the bulk. As such, the observed increased transition temperature results from the fact that the nanocrystals are immersed in the polymer matrix, making it necessary to go higher in temperature for the dispersed nanocrystals to make the ferroelectric–paraelectric transition temperature. The permittivity results also indicate a diffuse character of the phase transition, widened as compared with the bulk, induced by the small size of the MDABCO-NH_4I_3 nanocrystals [**41**,**42**] embedded in the polymer matrix.

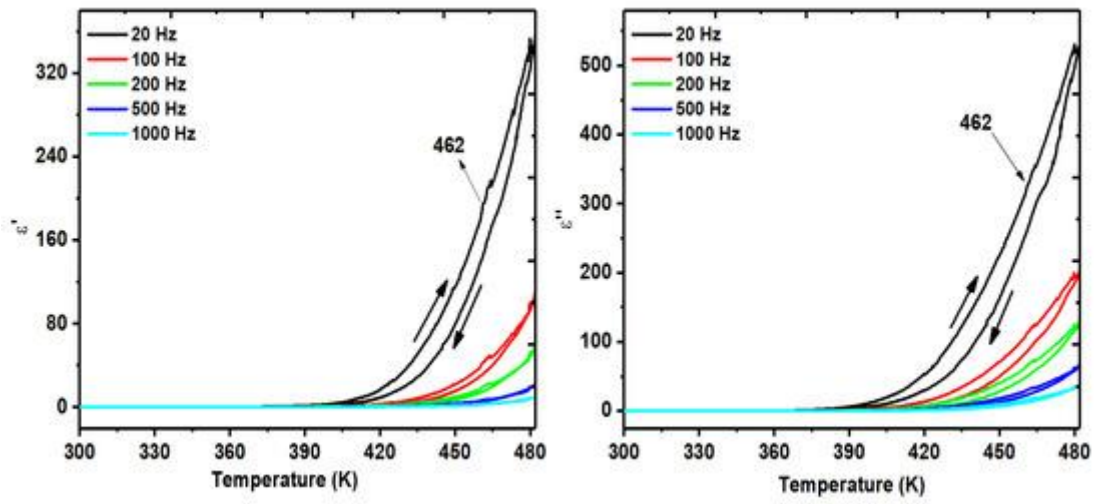

Figure 10. Dielectric permittivity of MDABCO-NH_4I_3 nanocrystals embedded in electrospun fibers, MDABCO-NH_4I_3@PA66a showing the ferroelectric–paraelectric phase transition at 462 K. In this figure, the up and down black arrows indicate respectively the heating and cooling cycles.

3.5. Pyroelectricity in Fibers

In this work, we report for the first time the measurement of the pyroelectric coefficient of polycrystalline MDABCO-NH_4I_3 perovskite (a pellet) and nanocrystals embedded in electrospun fibers of PA66, that is, MDABCO-NH_4I_3@PA66. Note that PA66 is the only polymer that allowed the pyroelectric measurement to be carried out since both PMMA and PVC melt before the perovskite phase-transition temperature is achieved. The measured coefficients, as a function of temperature, are shown in **Figure 11** for a fiber mat.

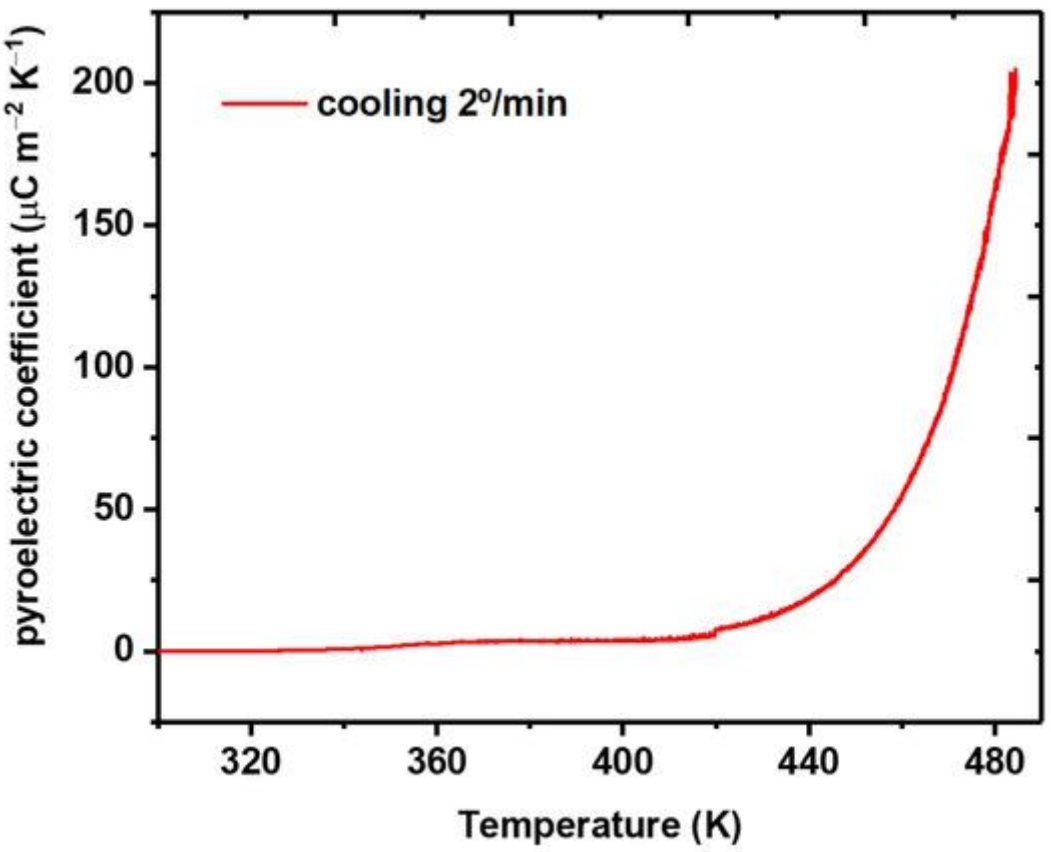

Figure 11. Pyroelectric coefficient as a function of the temperature of MDABCO-NH_4I_3@PA66 nanofibers, measured on cooling from the Curie transition temperature.

Extraordinarily, the pyroelectric coefficient of the MDABCO-NH_4I_3 nanocrystals increases to a very high value of 194 × 10^{-6} $Cm^{-2}k^{-1}$ achieved at 483 K, which is slightly above the Curie transition temperature value obtained for measurements of dielectric permittivity. This indicates a diffuse phase transition, which is expected to occur for nanocrystals randomly oriented inside a polymer matrix. The pyroelectric coefficient value obtained is within the same order of magnitude as that reported for the state-of-the-art semiorganic ferroelectric triglycine sulfate (TGS) single crystal, reported being 306 × 10^{-6} $Cm^{-2}k^{-1}$ at the ferroelectric–paraelectric phase transition [**43**].

3.6. Piezoelectric Voltage and Effective Piezoelectric Coefficients in Fibers

The behavior of the electrospun nanofiber mats fabricated from MDABCO-NH_4I_3@PA66, MDABCO-NH_4I_3@PMMA, and MDABCO-NH_4I_3@PVC is now studied as a piezoelectric energy generator. The generated open-circuit voltage, Voc, and short-circuit currents, Isc, are shown in **Figure 12** as functions of the external forces applied. In **Supplementary File, Figure S6**, the piezoelectric current generated by an MDABCO-NH_4I_3@PA66 fiber mat is shown. There is a linear relationship between the output electric current generated and the applied external forces, as expected

for a piezoelectric material. **Figure S7** shows the output voltage generated from the MDABCO-NH_4I_3@PVC nanofiber mat with reverse polarity. To analyze the reproducible behavior of the piezoelectric active nanofiber mat as a nanogenerator, a stability test was performed during a time interval of 4 h, uninterruptedly, under a periodical force applied with 2.7 N at a frequency of 3 Hz, **Figure S8**. The nanogenerator output voltage does not decrease over time. This is an important property indicating that the MDABCO-NH_4I_3 perovskite nanocrystals may be used to integrate future nanogenerators devices. For the MDABCO-NH_4I_3@PVC fiber mat, **Figure S9** shows the piezoelectric current generated during a time interval of 130 s under a periodical force applied with 4.5 N at a frequency of 3 Hz, as well as for frequencies between 1 Hz and 10 Hz.

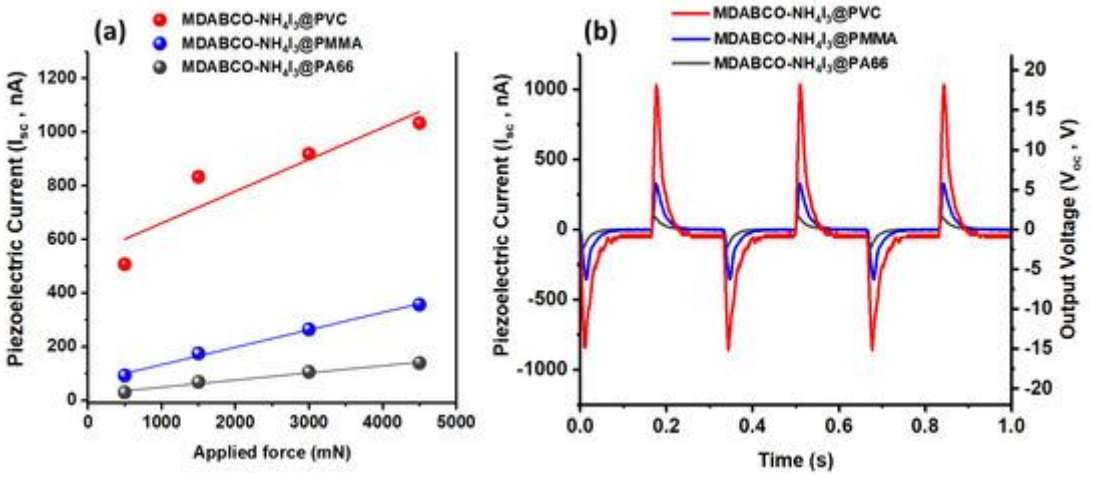

Figure 12. (**a**) Piezoelectric current as a function of the applied forces and (**b**) Output voltage and current as a function of time from MDABCO-NH_4I_3 incorporated into different electrospun polymer nanofibers.

The MDABCO-NH_4I_3@PVC nanofibers are very flexible and show a tensile strength and Young modulus of approximately 4.0 MPa and 58 MPa, respectively, as shown in **Figure S9**. Flexibility and high Young modulus are important characteristics for the performance of a fiber mat as a nanogenerator because they will increase its capacity to last for longer under an applied external force.

For a frequency of 3Hz and compression stress of 11 kPa, V_{oc} reaches 16.5 V for the PENG formed by the MDABCO-NH_4I_3@PVC nanofiber mat. For MDABCO-NH_4I_3@PMMA and MDABCO-NH_4I_3@PA66, V_{oc} reaches 6.1 V and 2.0 V, respectively. Low frequencies, such as 3Hz, are those that enable the generator to return to its original microscopic configuration before the next force is applied.

The charge generated by a piezoelectric mat, calculated from Q = ∫Idt (C), results in charge of 786 pC for the MDABCO-NH_4I_3@PVC mat considering a material response time of the order of 10^{-3} s and the maximum I_{sc} obtained of 786 nA. For MDABCO-NH_4I_3@PMMA and MDABCO-NH_4I_3@PA66 fiber mats, the charges generated are 288

pC and 95 pC, respectively. We may now calculate the effective piezoelectric coefficient, given by d_{eff} = Q/F (pCN^{-1}), for the three nanofiber mats under a periodical force applied at 4.5 N. These are 175 pCN^{-1}, 64 pCN^{-1}, and 21 pCN^{-1}, for MDABCO-NH_4I_3@PVC, MDABCO-NH_4I_3@PMMA, and MDABCO-NH_4I_3@PA66, respectively. The piezoelectric coefficient reported for a single MDABCO-NH_4I_3 crystal is d_{33} = 14 pCN^{-1} along the [1 1 1] direction of the crystal [**21**]. Therefore, the piezoelectric coefficient for the hybrid system formed by MDABCO-NH_4I_3 nanocrystals embedded in PVC fibers is one order of magnitude higher. Note that for this hybrid perovskite PENG, there is a small contribution from the piezoelectric polymer, which is piezoelectric (d_{31}~1.5 pCN^{-1}) [**44**]. The present result is consistent with the very high effective piezoelectric coefficient displayed by electrospun fibers incorporated with active organic piezoelectric materials, which has been previously reported for nonlinear optical organic crystal derivatives of nanocrystalline push–pull nitroaniline molecules and diphenylalanine dipeptides, when embedded in nano and microfibers fabricated by the electrospinning technique [**45**,**46**,**47**].

It is also important to calculate the peak power density, P = I_{sc}/A (μWm^{-2}) (A is the area of the electrode) delivered by the MDABCO-NH_4I_3@PVC nanofiber mat, which amounts to 1960 μWm^{-2}, two orders of magnitude higher than that reported for the methylammonium lead iodide ($CH_3NH_3PbI_3$) embedded into poly(vinylfluoride(PVDF) nanofibers, reported to be 12 μWm^{-2} for R_l = 10 MΩ [**30**]. Furthermore, our MDABCO-NH_4I_3@PVC piezoelectric generator is capable of delivering a peak power density with a magnitude similar to that achieved for electrically poled MDABCO-NH_4I_3 films deposited on a polyimide substrate after a preheating treatment up to 140 °C. Here, the piezoelectric generator delivered a peak power density of 2000 μWm^{-2} under an R_l = 250 MΩ [**48**]. Therefore, our electrospun-doped fiber mat can achieve a high peak power density without the need for electrical polling or previous heating treatment, which is very advantageous.

In the present work, we demonstrate that incorporating the organic lead-free perovskite MDABCO-NH_4I_3 into electrospun PVC fibers, processed at room temperature without poling, is an easy and straightforward way to fabricate piezoelectric generators using lead-free perovskite nanocrystals as active materials. Moreover, the piezoelectric voltage coefficient is defined as

$$g_{eff} = d_{eff}/(\varepsilon'\varepsilon_0)\ VmN^{-1}$$

which, as an important quantity for quantifying the performance of a material for integration as a piezoelectric sensor, was calculated for our electrospun fiber mats. For MDABCO-NH_4I_3@PVC, ε'= 50 at 20 Hz and g_{eff} = 3.6 VmN^{-1}. This extremely high piezoelectric voltage coefficient is one order of magnitude higher than that

displayed by a polyvinylidene fluoride (PVDF) polymer thin film for which g_{eff} = 0.29 VmN^{-1} [**49**,**50**] and six times higher than that exhibited by the layered lead perovskite $(4\text{-aminotetrahydropyran})_2PbBr_4$, which was reported to be g_{eff} = 0.67 VmN^{-1} [**11**].

4. Conclusions

In this study, we show that the lead-free organic ferroelectric perovskite N-methyl-N'-diazabicyclo[2.2.2]octonium)–ammonium triiodide (MDABCO-NH_4I_3) nanocrystals incorporated into electrospun fibers of three different polymers, processed at room temperature and without poling, can generate output voltages ranging from 2 V to ~17 V, using lead-free perovskite nanocrystals as active piezoelectric materials. In particular, we show that MDABCO-NH_4I_3 embedded in PVC fibers displays an effective piezoelectric voltage coefficient as high as g_{eff} =3.6 VmN^{-1}.

A piezoelectric nanogenerator (PENG) fabricated using an MDABCO-NH_4I_3@PVC electrospun fiber mat as the active piezoelectric component is demonstrated as a proof-of-concept. In addition, electrospun fibers exhibit intense blue photoluminescence at 325 nm, emitted by the embedded perovskite nanocrystals in the UV–vis–NIR and optical spectra. It is remarkable that MDABCO-NH_4I_3 inside the fibers show intense luminescence, which has not been reported before for this perovskite. Importantly, the pyroelectric coefficient of MDABCO-NH_4I_3 nanocrystals increases to the very high value of 194 × 10^{-6} $Cm^{-2}k^{-1}$ achieved at the ferroelectric–paraelectric transition. This pyroelectric coefficient has a magnitude within the same order as that reported for a semiorganic ferroelectric triglycine sulfate (TGS) single crystal. Additionally, the nanocrystals maintain their optical, piezoelectric, and pyroelectric properties for long periods when embedded into electrospun fibers, inhibiting perovskite oxidation, which is promoted by the polymer matrix that acts as a shielding.

Supplementary Materials

The following supporting information can be downloaded at: **https://www.mdpi.com/article/10.3390/ma15238397/s1**, Table S1: fit parameter values correspondent to Bragg reflection (111(111¯); Table S2: fit parameter values correspondent to Bragg reflection (200);200; Figure S1: asymmetric pseudo-Voigt fits; Figure S2: UV–vis reflectance; Figure S3: DSC spectra; Figure S4: Raman spectra; Figure S5: FTIR–ATR spectra; Figure S6: piezoelectric current; Figure S7: MDABCO-NH_4I_3@PVC nanofiber mat piezoelectric current with reverse polarity; Figure S8: piezoelectric current generated for frequencies between 1 Hz and 10 Hz, and stability test; Figure S9: elastic modulus, stress at yield, tensile strength, and strain at break. References [**50**,**51**,**52**,**53**,**54**] are cited in the Supplementary Materials.

Author Contributions

Conceptualization, R.M.F.B. and E.d.M.G.; investigation, R.M.F.B., G.M., B.A., B.S., J.O., P.V.R., A.M., C.C. and M.B.; writing—original draft preparation, R.M.F.B. and E.d.M.G.; writing—review and editing, R.M.F.B., E.d.M.G., B.A. and M.B.; supervision, R.M.F.B. and E.d.M.G.; project administration, R.M.F.B. and E.d.M.G.; funding acquisition, R.M.F.B. and E.d.M.G. All authors have read and agreed to the published version of the manuscript.

Funding

This research was funded by Fundação para a Ciência e Tecnologia through FEDER (European Fund for Regional Development)-COMPETE-QREN-EU (ref. UID/FIS/04650/2013 and UID/FIS/04650/2019) and E-Field—"Electric-Field Engineered Lattice Distortions (E-FiELD) for optoelectronic devices", ref. PTDC/NAN-MAT/0098/2020.

Institutional Review Board Statement

This study did not involve humans or animals.

Informed Consent Statement

This study did not involve humans or animals.

Acknowledgments

We acknowledge national funds (OE) through FCT—Fundação para a Ciência e a Tecnologia, I.P., in the scope of the framework contract foreseen in the numbers 4, 5, and 6 of article 23, of the Decree-Law 57/2016, of August 29, changed by Law 57/2017, of July 19.

Conflicts of Interest

The authors declare no conflict of interest.

References

1. Yuan, H.; Lei, T.; Qin, Y.; Yang, R. Flexible electronic skins based on piezoelectric nanogenerators and piezotronics. *Nano Energy* **2019**, *59*, 84–90.
2. Wang, Z.L. Towards Self-Powered Nanosystems: From Nanogenerators to Nanopiezotronics. *Adv. Funct. Mater.* **2008**, *18*, 3553–3567.
3. Valasek, J. Properties of Rochelle Salt Related to the Piezo-electric Effect. *Phys. Rev.* **1922**, *20*, 639–664.

4. Valasek, J. Piezo-Electric and Allied Phenomena in Rochelle Salt. *Phys. Rev.* **1921**, *17*, 475–481.

5. Lines, M.E.; Glass, A.M. *Principles and Applications of Ferroelectrics and Related Materials*; Oxford University Press: Oxford, UK, 2001; p. 694.

6. Scott James, F.; Paz de Araujo Carlos, A. Ferroelectric Memories. *Science* **1989**, *246*, 1400–1405.

7. Zhao, Z.; Dai, Y.; Dou, S.X.; Liang, J. Flexible nanogenerators for wearable electronic applications based on piezoelectric materials. *Mater. Today Energy* **2021**, *20*, 100690.

8. Sezer, N.; Koç, M. A comprehensive review on the state-of-the-art of piezoelectric energy harvesting. *Nano Energy* **2021**, *80*, 105567.

9. Cross, E. Lead-free at last. *Nature* **2004**, *432*, 24–25.

10. Saito, Y.; Takao, H.; Tani, T.; Nonoyama, T.; Takatori, K.; Homma, T.; Nagaya, T.; Nakamura, M. Lead-free piezoceramics. *Nature* **2004**, *432*, 84–87.

11. Chen, X.-G.; Song, X.-J.; Zhang, Z.-X.; Li, P.-F.; Ge, J.-Z.; Tang, Y.-Y.; Gao, J.-X.; Zhang, W.-Y.; Fu, D.-W.; You, Y.-M.; et al. Two-Dimensional Layered Perovskite Ferroelectric with Giant Piezoelectric Voltage Coefficient. *J. Am. Chem. Soc.* **2020**, *142*, 1077–1082.

12. Guo, T.-M.; Gong, Y.-J.; Li, Z.-G.; Liu, Y.-M.; Li, W.; Li, Z.-Y.; Bu, X.-H. A New Hybrid Lead-Free Metal Halide Piezoelectric for Energy Harvesting and Human Motion Sensing. *Small* **2022**, *18*, 2103829.

13. Zhang, H.-Y.; Tang, Y.-Y.; Shi, P.-P.; Xiong, R.-G. Toward the Targeted Design of Molecular Ferroelectrics: Modifying Molecular Symmetries and Homochirality. *Acc. Chem. Res.* **2019**, *52*, 1928–1938.

14. Li, W.; Wang, Z.; Deschler, F.; Gao, S.; Friend, R.H.; Cheetham, A.K. Chemically diverse and multifunctional hybrid organic–inorganic perovskites. *Nat. Rev. Mater.* **2017**, *2*, 16099.

15. Song, X.; Hodes, G.; Zhao, K.; Liu, S. Metal-Free Organic Halide Perovskite: A New Class for Next Optoelectronic Generation Devices. *Adv. Energy Mater.* **2021**, *11*, 2003331.

16. Chu, L.-L.; Zhang, T.; Zhang, W.-Y.; Shi, P.-P.; Gao, J.-X.; Ye, Q.; Fu, D.-W. Three-Dimensional Metal-Free Molecular Perovskite with a Thermally Induced Switchable Dielectric Response. *J. Phys. Chem. Lett.* **2020**, *11*, 1668–1674.

17. You, Y.-M.; Liao, W.-Q.; Zhao, D.; Ye, H.-Y.; Zhang, Y.; Zhou, Q.; Niu, X.; Wang, J.; Li, P.-F.; Fu, D.-W.; et al. An organic-inorganic perovskite ferroelectric with large piezoelectric response. *Science* **2017**, *357*, 306–309.

18. Saparov, B.; Mitzi, D.B. Organic–Inorganic Perovskites: Structural Versatility for Functional Materials Design. *Chem. Rev.* **2016**, *116*, 4558–4596.

19. Kamat, P.V.; Bisquert, J.; Buriak, J. Lead-Free Perovskite Solar Cells. *ACS Energy Lett.* **2017**, *2*, 904–905.

20. Boix, P.P.; Agarwala, S.; Koh, T.M.; Mathews, N.; Mhaisalkar, S.G. Perovskite Solar Cells: Beyond Methylammonium Lead Iodide. *J. Phys. Chem. Lett.* **2015**, *6*, 898–907.

21. Ye, H.-Y.; Tang, Y.-Y.; Li, P.-F.; Liao, W.-Q.; Gao, J.-X.; Hua, X.-N.; Cai, H.; Shi, P.-P.; You, Y.-M.; Xiong, R.-G. Metal-free three-dimensional perovskite ferroelectrics. *Science* **2018**, *361*, 151–155.

22. Wang, H.; Liu, H.; Zhang, Z.; Liu, Z.; Lv, Z.; Li, T.; Ju, W.; Li, H.; Cai, X.; Han, H. Large piezoelectric response in a family of metal-free perovskite ferroelectric compounds from first-principles calculations. *npj Comput. Mater.* **2019**, *5*, 17.

23. Doshi, J.; Reneker, D.H. Electrospinning process and applications of electrospun fibers. *J. Electrostat.* **1995**, *35*, 151–160.

24. Reneker, D.H.; Chun, I. Nanometre diameter fibres of polymer, produced by electrospinning. *Nanotechnology* **1996**, *7*, 216–223.

25. Ramakrishna, S.; Fujihara, K.; Teo, W.-E.; Yong, T.; Ma, Z.; Ramaseshan, R. Electrospun nanofibers: Solving global issues. *Mater. Today* **2006**, *9*, 40–50.

26. Isakov, D.V.; de Matos Gomes, E.; Vieira, L.G.; Dekola, T.; Belsley, M.S.; Almeida, B.G. Oriented single-crystal-like molecular arrangement of optically nonlinear 2-methyl-4-nitroaniline in electrospun nanofibers. *ACS Nano* **2011**, *5*, 73–78.

27. Richard-Lacroix, M.; Pellerin, C. Molecular Orientation in Electrospun Fibers: From Mats to Single Fibers. *Macromolecules* **2013**, *46*, 9473–9493.

28. Rørvik, P.M.; Grande, T.; Einarsrud, M.-A. One-Dimensional Nanostructures of Ferroelectric Perovskites. *Adv. Mater.* **2011**, *23*, 4007–4034.

29. Isakov, D.; de Matos Gomes, E.; Almeida, B.; Kholkin, A.L.; Zelenovskiy, P.; Neradovskiy, M.; Shur, V.Y. Energy harvesting from nanofibers of hybrid organic ferroelectric dabcoHReO$_4$. *Appl. Phys. Lett.* **2014**, *104*, 032907.

30. Sultana, A.; Ghosh, S.K.; Alam, M.M.; Sadhukhan, P.; Roy, K.; Xie, M.; Bowen, C.R.; Sarkar, S.; Das, S.; Middya, T.R.; et al. Methylammonium Lead Iodide Incorporated Poly(vinylidene fluoride) Nanofibers for Flexible Piezoelectric–Pyroelectric Nanogenerator. *ACS Appl. Mater. Inter.* **2019**, *11*, 27279–27287.

31. Marino, M.G.; Kreuer, K.D. Alkaline Stability of Quaternary Ammonium Cations for Alkaline Fuel Cell Membranes and Ionic Liquids. *ChemSusChem* **2015**, *8*, 513–523.

32. Sá, P.; Barbosa, J.; Bdikin, I.; Almeida, B.; Rolo, A.G.; Gomes, E.d.M.; Belsley, M.; Kholkin, A.L.; Isakov, D. Ferroelectric characterization of aligned barium titanate nanofibres. *J. Phys. D Appl. Phys.* **2013**, *46*, 105304.

33. Kubelka, P. New Contributions to the Optics of Intensely Light-Scattering Materials. Part I. *J. Opt. Soc. Am.* **1948**, *38*, 448–457.

34. Makuła, P.; Pacia, M.; Macyk, W. How To Correctly Determine the Band Gap Energy of Modified Semiconductor Photocatalysts Based on UV–Vis Spectra. *J. Phys. Chem. Lett.* **2018**, *9*, 6814–6817.

35. Song, X.; Li, Q.; Han, J.; Ma, C.; Xu, Z.; Li, H.; Wang, P.; Yang, Z.; Cui, Q.; Gao, L.; et al. Highly Luminescent Metal-Free Perovskite Single Crystal for Biocompatible X-Ray Detector to Attain Highest Sensitivity. *Adv. Mater.* **2021**, *33*, 2102190.

36. Kasel, T.W.; Deng, Z.; Mroz, A.M.; Hendon, C.H.; Butler, K.T.; Canepa, P. Metal-free perovskites for non linear optical materials. *Chem. Sci.* **2019**, *10*, 8187–8194.

37. Sirbu, D.; Tsui, H.C.L.; Alsaif, N.; Iglesias-Porras, S.; Zhang, Y.; Wang, M.; Liu, M.; Peacock, A.C.; Docampo, P.; Healy, N. Wide-Band-Gap Metal-Free Perovskite for Third-Order Nonlinear Optics. *ACS Photonics* **2021**, *8*, 2450–2458.

38. Zhao, Z.; Buscaglia, V.; Viviani, M.; Buscaglia, M.T.; Mitoseriu, L.; Testino, A.; Nygren, M.; Johnsson, M.; Nanni, P. Grain-size effects on the ferroelectric behavior of dense nanocrystalline $BaTiO_3$ ceramics. *Phys. Rev. B* **2004**, *70*, 024107.

39. Choi, K.J.; Biegalski, M.; Li, Y.L.; Sharan, A.; Schubert, J.; Uecker, R.; Reiche, P.; Chen, Y.B.; Pan, X.Q.; Gopalan, V.; et al. Enhancement of Ferroelectricity in Strained $BaTiO_3$ Thin Films. *Science* **2004**, *306*, 1005–1009.

40. Belhadi, J.; El Marssi, M.; Gagou, Y.; Yuzyuk, Y.I.; Raevski, I.P. Giant increase of ferroelectric phase transition temperature in highly strained ferroelectric $[BaTiO_3]0.7Λ/[BaZrO_3]0.3Λ$ superlattice. *Europhys. Lett.* **2014**, *106*, 17004.

41. Petzelt, J. Dielectric Grain-Size Effect in High-Permittivity Ceramics. *Ferroelectrics* **2010**, *400*, 117–134.

42. Mao, C.; Yan, S.; Cao, S.; Yao, C.; Cao, F.; Wang, G.; Dong, X.; Hu, X.; Yang, C. Effect of grain size on phase transition, dielectric and pyroelectric properties of BST ceramics. *J. Eur. Ceram. Soc.* **2014**, *34*, 2933–2939.

43. Ghane-Motlagh, R.; Kroener, M.; Goldschmidtboeing, F.; Danilewsky, A.N.; Woias, P. A dynamic method for the measurement of pyroelectric properties of materials. *Smart Mater. Struct.* **2018**, *27*, 084004.

44. Bharti, V.; Kaura, T.; Nath, R. Improved piezoelectricity in solvent-cast PVC films. *IEEE Trans. Dielectr. Electr. Insul.* **1995**, *2*, 1106–1110.

45. Baptista, R.M.F.; Lopes, P.E.; Rodrigues, A.R.O.; Cerca, N.; Belsley, M.S.; de Matos Gomes, E. Self-assembly of Boc-p-nitro-l-phenylalanyl-p-nitro-l-phenylalanine and Boc-l-phenylalanyl-l-tyrosine in solution and into piezoelectric electrospun fibers. *Mater. Adv.* **2022**, *3*, 2934–2944.

46. Baptista, R.M.F.; de Matos Gomes, E.; Raposo, M.M.M.; Costa, S.P.G.; Lopes, P.E.; Almeida, B.; Belsley, M.S. Self-assembly of dipeptide Boc-diphenylalanine nanotubes inside electrospun polymeric fibers with strong piezoelectric response. *Nanoscale Adv.* **2019**, *1*, 4339–4346.

47. Bernardo, C.R.; Baptista, R.M.F.; de Matos Gomes, E.; Lopes, P.E.; Raposo, M.M.M.; Costa, S.P.G.; Belsley, M.S. Anisotropic PCL nanofibers embedded with nonlinear nanocrystals as strong generators of polarized second harmonic light and piezoelectric currents. *Nanoscale Adv.* **2020**, *2*, 1206–1213.

48. Wu, H.-S.; Wei, S.-M.; Chen, S.-W.; Pan, H.-C.; Pan, W.-P.; Huang, S.-M.; Tsai, M.-L.; Yang, P.-K. Metal-Free Perovskite Piezoelectric Nanogenerators for Human–Machine Interfaces and Self-Powered Electrical Stimulation Applications. *Adv. Sci.* **2022**, *9*, 2105974.

49. Li, M.; Wondergem, H.J.; Spijkman, M.-J.; Asadi, K.; Katsouras, I.; Blom, P.W.M.; de Leeuw, D.M. Revisiting the δ-phase of poly(vinylidene fluoride) for solution-processed ferroelectric thin films. *Nat. Mater.* **2013**, *12*, 433–438.

50. Klug, H.; Alexander, L. *X-Ray Diffraction Procedures*, 2nd ed.; Ch. 9; Wiley: Hoboken, NJ, USA, 1974. [

51. D'Errico, J. SLM—Shape Language Modeling. MATLAB Central File Exchange. 2022.

52. Stancik, A.L.; Brauns, E.B. A simple asymmetric lineshape for fitting infrared absorption spectra. *Vib. Spectrosc.* **2008**, *47*, 66–69.

53. Keve, E.T.; Abrahams, S.C.; Bernstein, J.L. Pyroelectric Ammonium Iodate, a Potential Ferroelastic: Crystal Structure. *J. Chem. Phys.* **1971**, *54*, 2556–2563.

54. Lee, D.W.; De Los Santos, V.L.; Seo, J.W.; Félix, L.L.; Bustamante, D.A.; Cole, J.M.; Barnes, C.H.W. The Structure of Graphite Oxide: Investigation of Its Surface Chemical Groups. *J. Phys. Chem. B* **2010**, *114*, 5723–5728.

Supplementary Information

SI1. XRD crystallites size

Estimates of the nanocrystal size, d, was obtained using the Scherrer equation

$$\beta_{hkl} = \frac{K\lambda}{dcos\theta} \qquad (1)$$

Here K is a correction factor to particle shape and λ the X-ray wavelength. In the absence of detailed shape information, a value of $K = 0.90$ is commonly used [1]. The full width of the diffraction peak at half the maximum (FWHM) gives the broadening of a (hkl) reflection and is expressed as β_{hkl}. To estimate the FWHM, first the main peaks were eliminated from the spectra and a cubic spline was globally fit to the resulting background using the MATLAB application "shape language modeling" [2].

Subsequently each individual background corrected peak was fit to and asymmetric Pseudo-Voight profile using the MATLAB nonlinear least squares fitting algorithm. The Pseudo-Voigt function is,

$$I = A\left[\eta L(x) + (1-\eta)G(x)\right] \qquad (2)$$

Representing a weighted linear superposition of Lorentz $L(x)$ and Gauss $G(x)$ functions. Here the parameter η represents the fractional contribution of the Lorentz function while the parameter A is proportional to the amplitude of the

diffraction peak above the background. The Lorentzian and Gaussian functions are:

$$L(x) = \frac{\left(2/\pi\beta^*\right)}{1+4x^2}$$
$$G(x) = \frac{2}{\beta^*}\sqrt{\frac{\ln(2)}{\pi}}\exp(-4\ln(2)x^2) \qquad (2a)$$

written in terms of the scaled diffraction angle

$$x = \frac{2\left(2\theta - 2\theta_c\right)}{\beta^*} \qquad (2b)$$

and the asymmetric width function [3]

$$\beta^* = \frac{2\beta}{1+\exp\left[a\left(2\theta - 2\theta_c\right)\right]} \qquad (2c)$$

In these expressions, the calculated peak position is $2\theta_c$ and a represents the asymmetry parameter.

The resulting fits are shown in Figure S1 a) to) while Tables S1 and S2 list the fit parameter values $(A,\eta,\theta_c,\beta,a)$ for the two peaks $(11\bar{1})$ and (200). The red shading in Figure S1 represents the 68% confidence intervals of the fit peaks.

Table S1: Fit parameter values for the MDABCO-NH_4I_3 embedded into PVC, PA66 and PMMA correspondent to Bragg reflection $(11\bar{1})$.

	A	η	$2\theta_c$	β	a
MDABCO-NH_4I_3@ PVC	9.02	1.00	21.947º	0.124º	-6.35
MDABCO-NH_4I_3@ PA66	12.639	1.00	21.941º	0.099º	-2.45
MDABCO-NH_4I_3@ PMMA	19.50	1.00	21.883	0.100º	4.846

Table S2: Fit parameter values for the MDABCO-NH_4I_3 embedded into PVC, PA66 and PMMA correspondent to Bragg reflection (200).

	A	η	$2\theta_c$	β	a
MDABCO-NH_4I_3@ PVC	12.84	0.60	24.676º	0.158º	16.51
MDABCO-NH_4I_3@ PA66	9.07	1.00	24.702º	0.103º	6.37
MDABCO-NH_4I_3@ PMMA	14.10	0.65	24.649º	0.121º	3.53

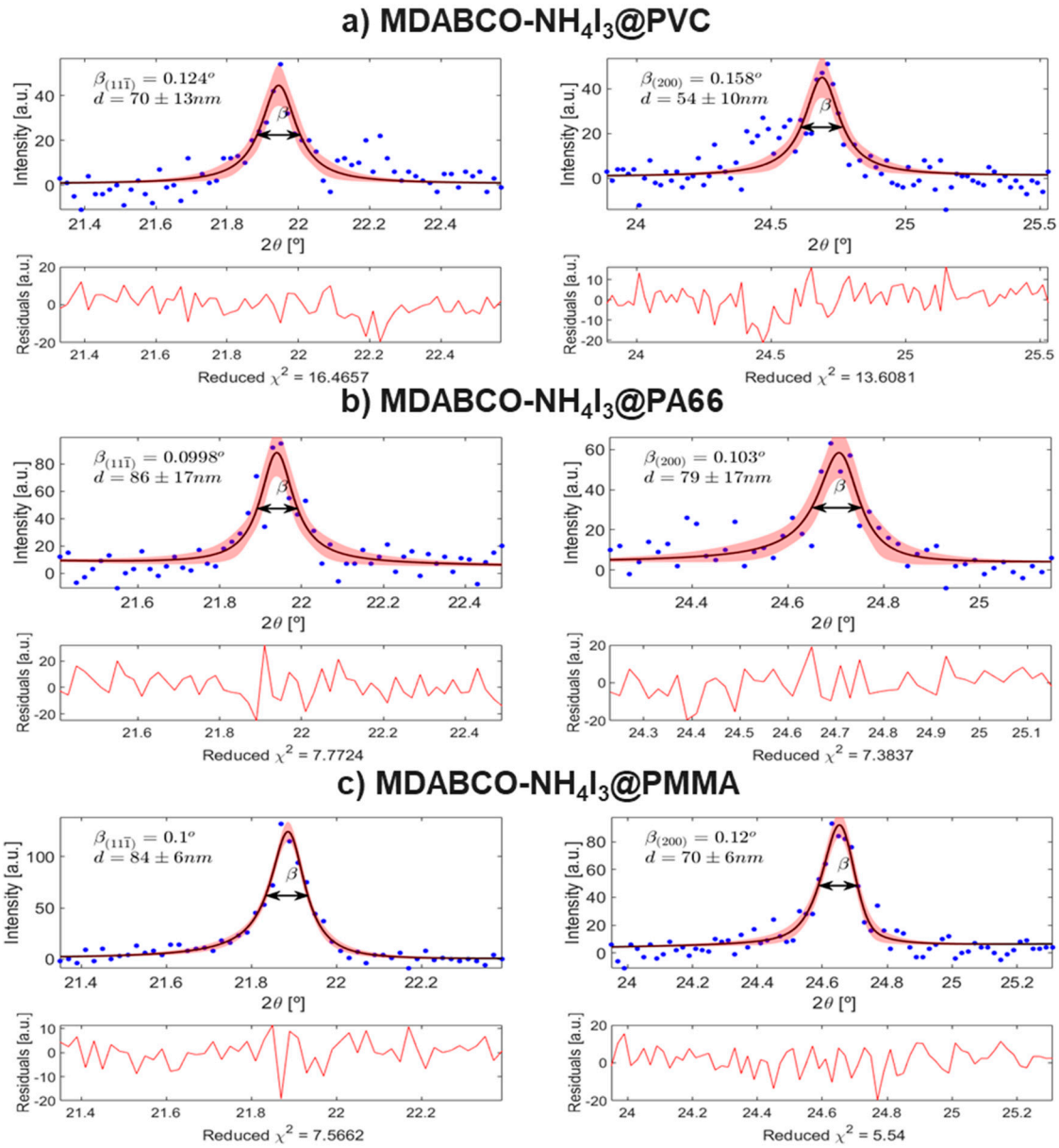

Figure S1. Asymmetric Pseudo-Voigt fits of the (11$\bar{1}$) and (200) Bragg reflections for MDABCO-NH_4I_3 crystals inside a) PVC, b) PA66 and c) PMMA nanofibers. The width of the reflections at half the maximum β and the nanocrystals average size d is indicated as well the refit residuals.

S2. UV-Visible Reflectance Spectra

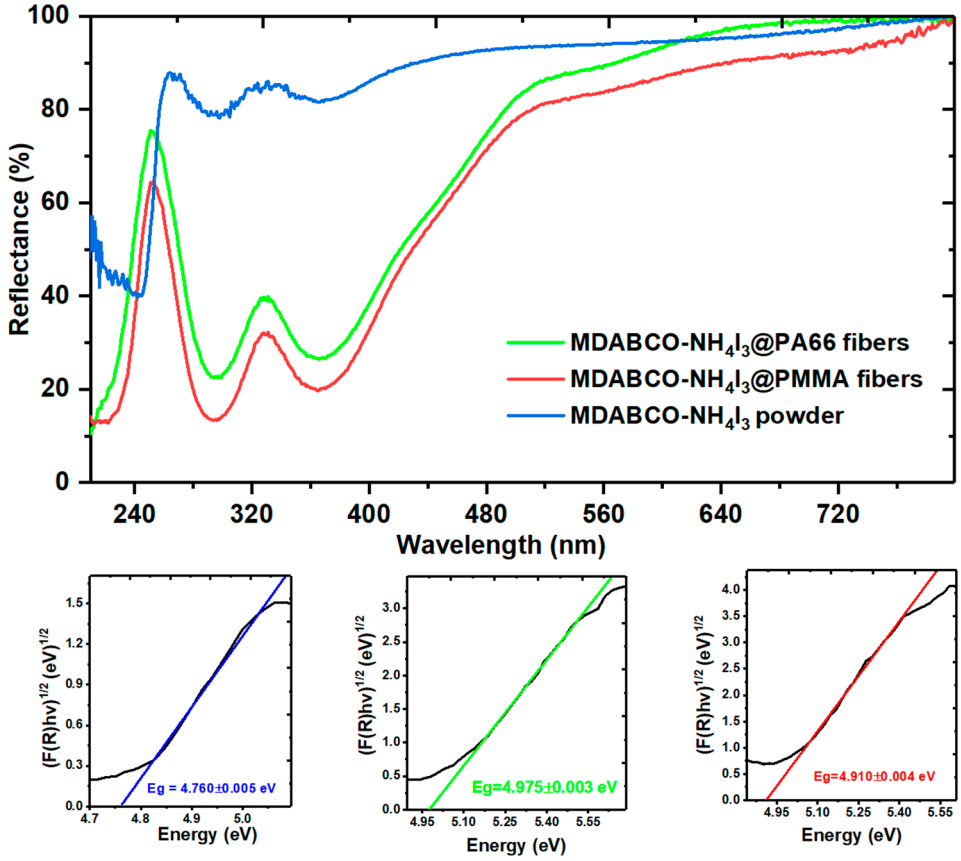

Figure S2. UV–vis reflectance of MDABCO-NH_4I_3 powder pellet and electrospun fibers. The inset shows the Kubelka-Munk function indicating a band gap energy of 4.760 eV for the polycrystalline perovskite, 4.975 eV and 4.910 eV for MDABCO-NH_4I_3@PA66 and MDABCO-NH_4I_3@PMMA nanofibers, respectively.

S3. DSC analysis

In figure S3, the measured DSC of synthesized MDABCO-NH_4I_3 perovskite crystals, showed the ferroelectric-paraelectric phase transition to occur at 443 K with area 19.9 J/g. MDABCO-NH_4I_3 perovskite crystals start to decompose above 460 K with the formation of NH_4IO_3. Cooling down from 473 K, shows a peak at 350 K, area -13.26 J/g. During the second heating, a peak with maximum at 358 K and area 12.3 J/g is observed. These two peaks correspond respectively to the paraelectric to ferroelectric and ferroelectric-paraelectric phase transitions of

NH_4IO_3 compound, which was formed after the first heating [4]. The perovskite phase transition at 443 K is not recovered, which reveals that crystal thermal degradation starts above 460 K[5].

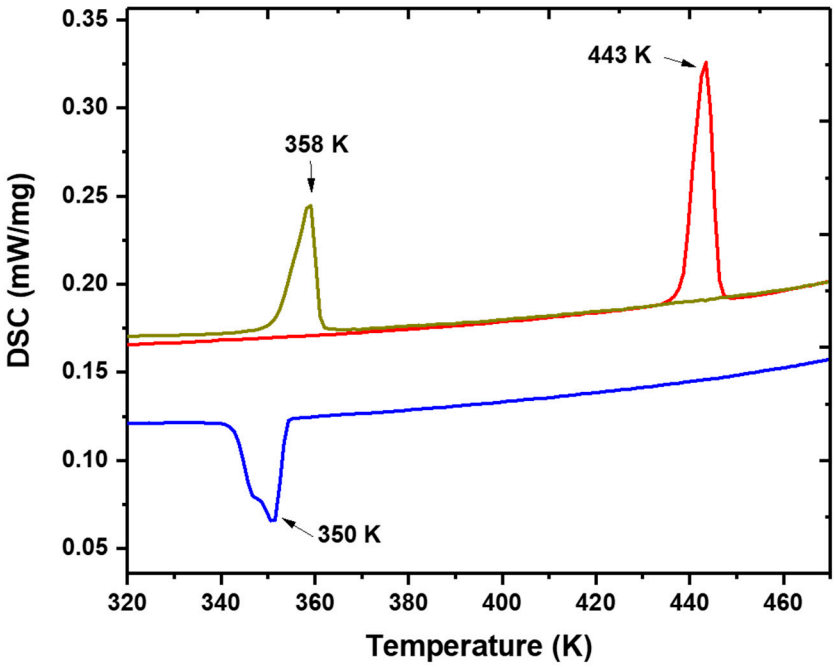

Figure S3. DSC spectra of synthesized MDABCO-NH_4I_3 perovskite crystals.

S4. RAMAN Spectra

In Figure S4, the measured Raman modes between $50 - 600\ cm^{-1}$ are shown for a MDABCO-NH_4I_3 polycrystalline sample, for electrospun fibers of PVC and MDABCO-NH_4I_3@PVC. In the spectra, the low frequency modes are due to lattice vibrations. From the two bands at $68\ cm^{-1}$ and $103\ cm^{-1}$ present in the polycrystalline sample, only the second band (now shifted to $109\ cm^{-1}$) remains intense for the perovskite nanocrystals embedded in the polymer fibers. The strong decreasing in intensity of the $68\ cm^{-1}$ band is probably the result of constrains imposed by the polymer matrix on the lattice vibrations modes, due to crystal confinement.

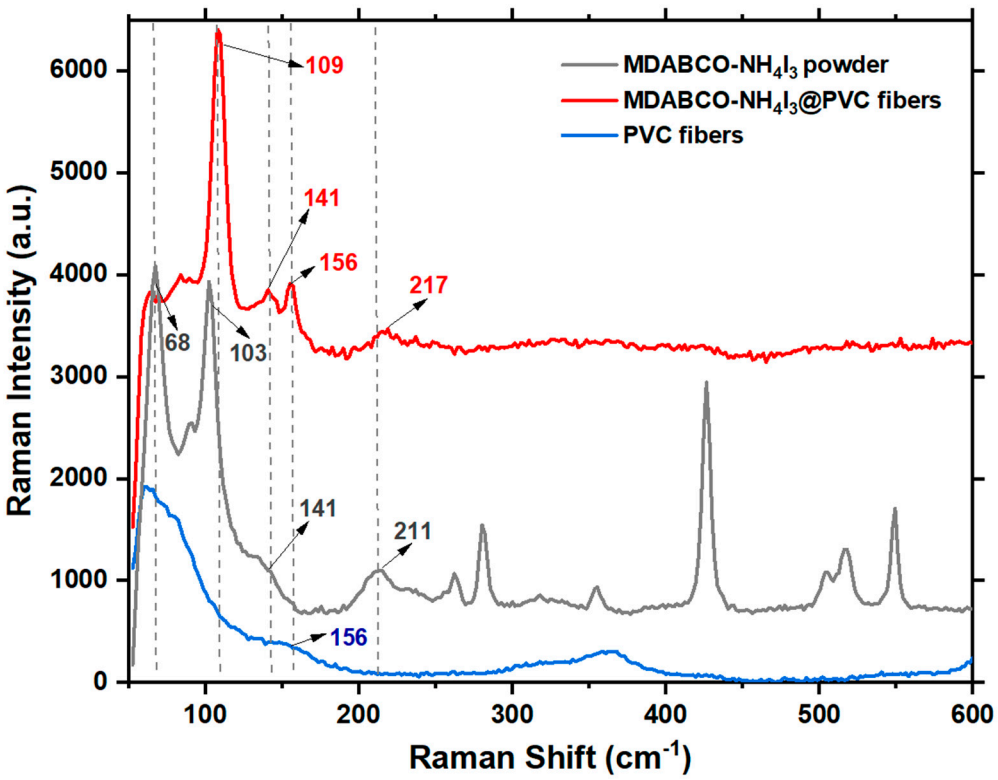

Figure S4. Raman spectra for MDABCO-NH_4I_3 polycrystalline sample (black line), for electrospun fibers of PVC (blue line) and MDABCO-NH_4I_3@PVC fibers (red line), expansion between $50 - 600\ cm^{-1}$.

The weak broad bands centred at 141 cm^{-1} for polycrystalline MDABCO-NH_4I_3 and 156 cm^{-1} for PVC fibers, are resolved into well-defined bands for MDABCO-NH_4I_3@PVC fibers. The weak band for MDABCO-NH_4I_3 at 211 cm^{-1} is slightly shifted to 217 cm^{-1}, for the perovskite incorporated into the fibers.

Noticed that for MDABCO-NH_4I_3@PVC fibers, none of the Raman peaks between $250 - 600\ cm^{-1}$ are perceptible, while they are present in the MDABCO-NH_4I_3 perovskite spectra. We may conclude that the polymer matrix strongly constrains these perovskite vibrational modes as mentioned above, which is expectable as the fibers were electrospun from a precursor solution with ration of MDABCO-NH_4I_3 to PVC of 1:5.

S5. FTIR-ATR analysis

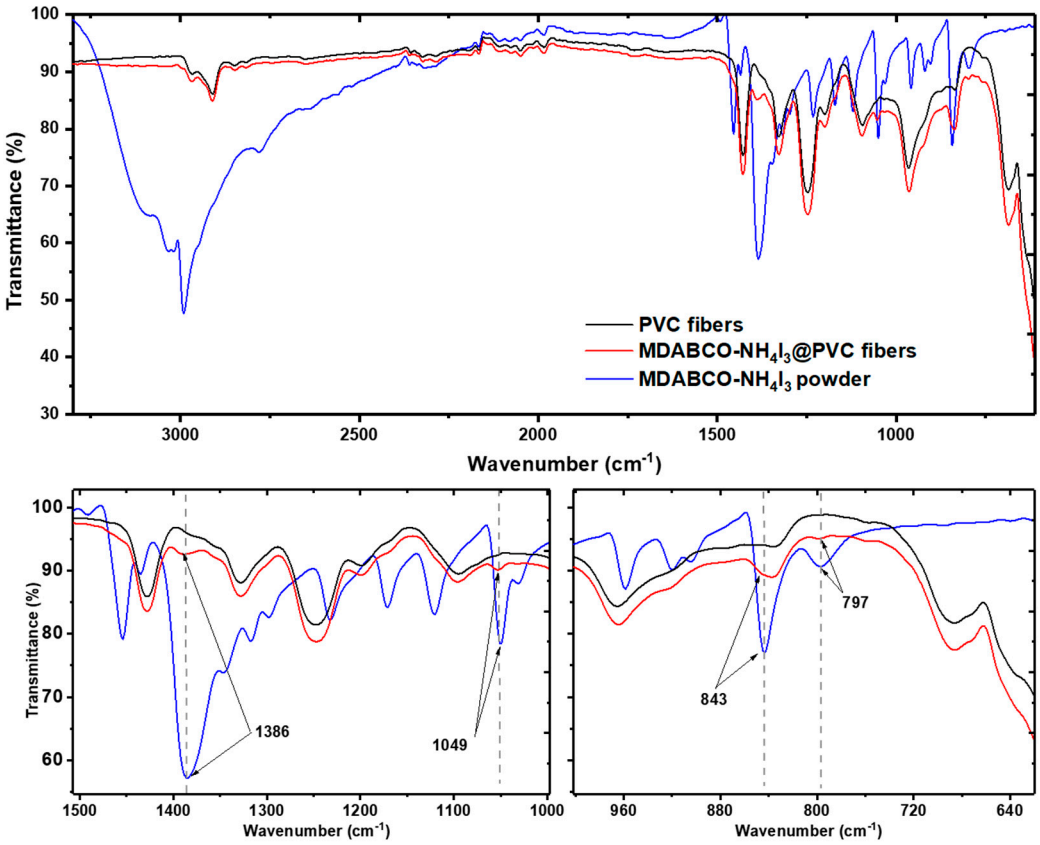

Figure S5. FTIR-ATR spectra of PVC polymer, MDABCO-NH_4I_3 powder and MDABCO-NH_4I_3@PVC fibers, a) full measurement and b) expansion between $1000 - 1500\ cm^{-1}$ and $600 - 1000\ cm^{-1}$.

In Figure S5 b), the measured FTIR-ATR between $1500 - 600\ cm^{-1}$ is shown for a MDABCO-NH_4I_3 polycrystalline sample, for electrospun fibers of PVC and MDABCO-NH_4I_3@PVC. Slight differences were observed between the spectra of electrospun fibers of PVC and MDABCO-NH_4I_3@PVC, and just few bands (the most intense) were possible to be assigned to MDABCO-NH_4I_3 perovskite nanocrystals at the 1386 cm^{-1}, 1049 cm^{-1}, 843 cm^{-1} and 797 cm^{-1}. However, the strong decreasing in intensity observed for the perovskite bands on electrospun fibers of MDABCO-NH_4I_3@PVC sample is due to the sobreposition of the polymer bands to those of MDABCO-NH_4I_3 crystals. As already mentioned, the ratio perovskite and polymer are 1:5, on the precursor solution used to fabricate

the electrospun fibers. Therefore, is expected that the only the stronger perovskite bands will be observed. That contained a concentration constrain imposed by the polymer matrix on the IR bands.

S6. Piezoelectric nanogenerator

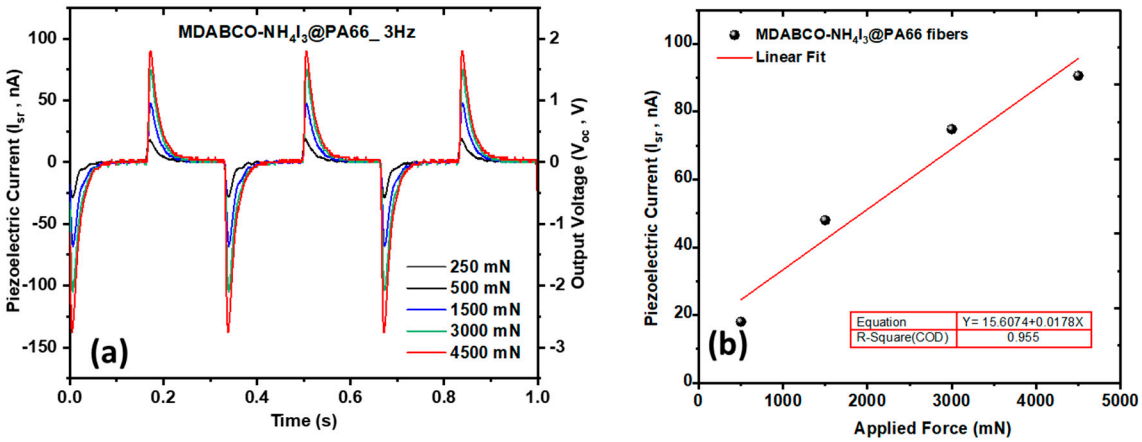

Figure S6. MDABCO-NH_4I_3@PA66 fibers (a) Piezoelectric current as function of time, for several applied forces and (b) linear fitting.

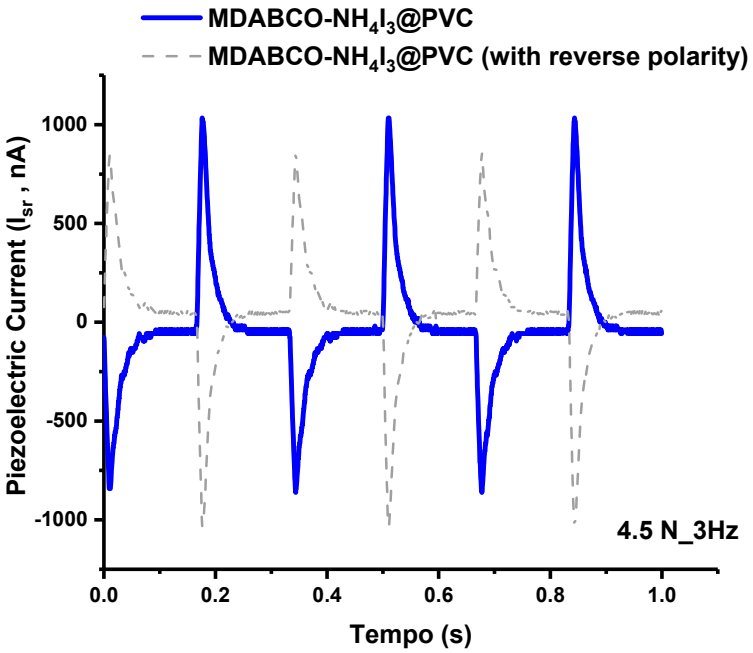

Figure S7. Output voltage generated from MDABCO-NH_4I_3@PVC nanofiber mat with reverse polarity.

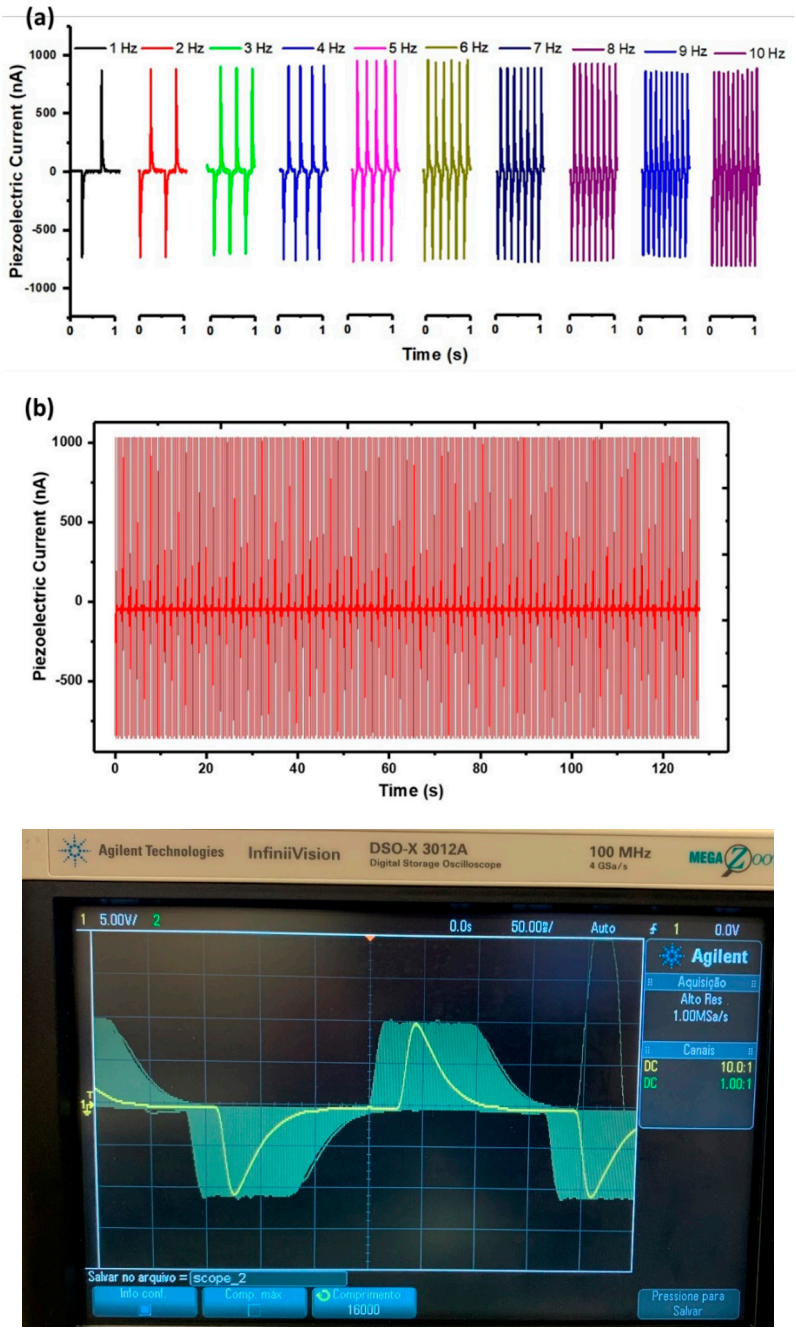

Figure S8. MDABCO-NH_4I_3@PVC nanofiber mat piezoelectric current generated a) for frequencies between 1Hz and 10 Hz and b) a 130 s interval under a periodical force applied with 4.5 N. A stability test was performed during a time interval of 4 h under a periodical force applied with 2.7 N at a frequency of 3 Hz (oscilloscope image).

S9. Mechanical Properties

Tensile strain applied to PVC and MDABCO-NH_4I_3@PVC electrospun fiber mat are shown in Figure S9. The results from tensile measurements show that MDABCO-NH_4I_3@PVC fibers exhibit good mechanical performance with an average increase of 14% on tensile strength (reaching ~ 4.0 MPa) and an increase of 40% on the strength at yield reaching (~ 2.5 MPa) when compared with PVC fibers. More importantly, the Young modulus increases from ~20 MPa in PVC fibers to ~58 MPa in MDABCO-NH_4I_3@PVC fibers, an increase of around 66%. This significant increase of the Young modulus of perovskite doped electrospun fibers indicates that composite MDABCO-NH_4I_3@PVC are mechanically stronger than neat polymer fibers. This is very important for the performance of MDABCO-NH_4I_3@PVC fiber mat as nanogenerator as it will increase its capability of supporting longer times under applied external force.

The decrease of 30% on the strain at break for doped fibers indicates a decrease in their plasticity, which might result from the presence of nanocrystals inside the PVC polymer which inhibits the capability for the PVC chains to flow between.[6]

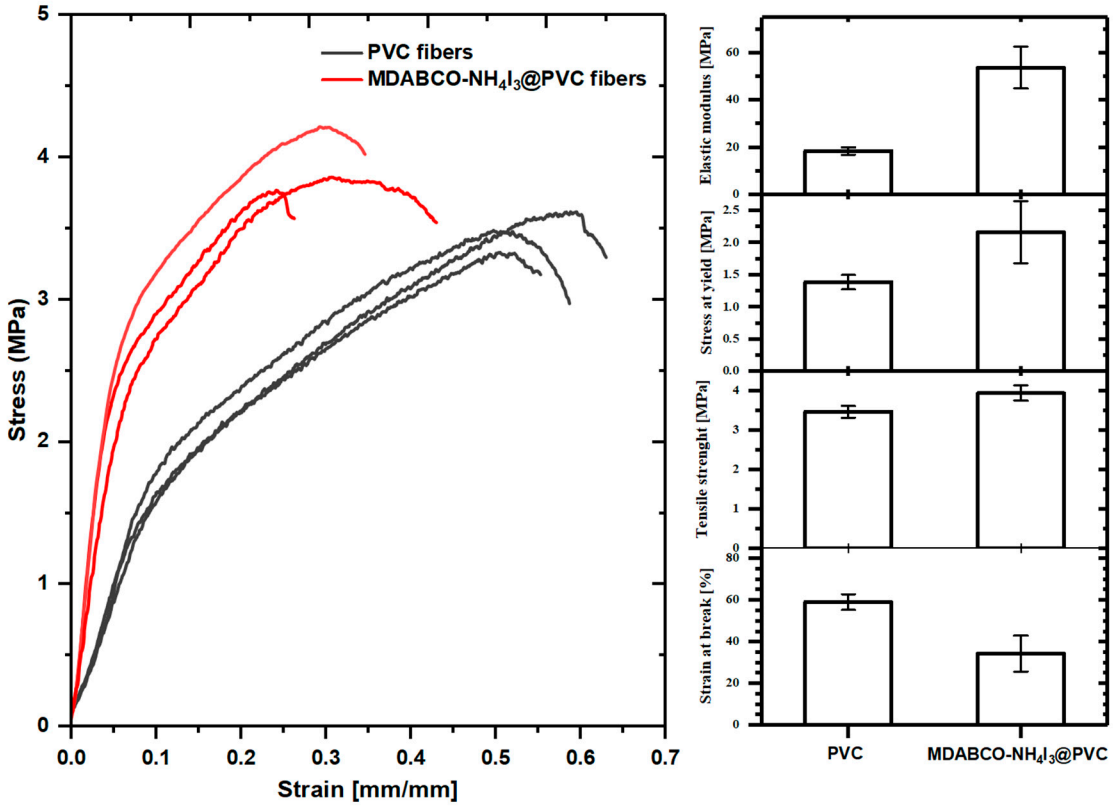

Figure S9. Elastic modulus, stress at yield, tensile strength and strain at break of PVC and MDABCO-NH_4I_3@PVC electrospun fibers.

References

(1) Klug, H.; Alexander, L., *X-Ray Diffraction Procedures 2nd edn*, Ch. 9. Wiley: 1974.

(2) John D'Errico (2022). SLM - Shape Language Modeling. https://www.mathworks.com/matlabcentral/fileexchange/24443-slm-shape-language-modeling), MATLAB Central File Exchange. Retrieved July 5, 2022.

(3) Stancik, A. L.; Brauns, E. B. A simple asymmetric lineshape for fitting infrared absorption spectra. *Vib Spectrosc* **2008,** *47* (1), 66-69, DOI: https://doi.org/10.1016/j.vibspec.2008.02.009.

(4) Keve, E. T.; Abrahams, S. C.; Bernstein, J. L. Pyroelectric Ammonium Iodate, a Potential Ferroelastic: Crystal Structure. *The Journal of Chemical Physics* **1971,** *54* (6), 2556-2563, https://doi.org/10.1063/1.1675212.

(5) Sirbu, D.; Tsui, H. C. L.; Alsaif, N.; Iglesias-Porras, S.; Zhang, Y.; Wang, M.; Liu, M.; Peacock, A. C.; Docampo, P.; Healy, N. Wide-Band-Gap Metal-Free Perovskite for Third-Order Nonlinear Optics. *Acs Photonics* **2021,** *8* (8), 2450-2458, https://doi.org/10.1021/acsphotonics.1c00687.

(6) Lee, D. W.; De Los Santos V, L.; Seo, J. W.; Felix, L. L.; Bustamante D, A.; Cole, J. M.; Barnes, C. H. W. The Structure of Graphite Oxide: Investigation of Its Surface Chemical Groups. *The Journal of Physical Chemistry B* **2010,** *114* (17), 5723-5728, https://doi.org/10.1021/jp1002275.